Article

Iron-based binary ferromagnets for transverse thermoelectric conversion

https://doi.org/10.1038/s41586-020-2230-z

Received: 26 July 2019

Accepted: 4 February 2020

Published online: 27 April 2020

Check for updates

Akito Sakai[1,2,3,10], Susumu Minami[4,5,10], Takashi Koretsune[6,10], Taishi Chen[1,3,10], Tomoya Higo[1,3,10], Yangming Wang[1], Takuya Nomoto[7], Motoaki Hirayama[5], Shinji Miwa[1,3,8], Daisuke Nishio-Hamane[1], Fumiyuki Ishii[4,5], Ryotaro Arita[3,5,7] & Satoru Nakatsuji[1,2,3,8,9]✉

Thermoelectric generation using the anomalous Nernst effect (ANE) has great potential for application in energy harvesting technology because the transverse geometry of the Nernst effect should enable efficient, large-area and flexible coverage of a heat source. For such applications to be viable, substantial improvements will be necessary not only for their performance but also for the associated material costs, safety and stability. In terms of the electronic structure, the anomalous Nernst effect (ANE) originates from the Berry curvature of the conduction electrons near the Fermi energy[1,2]. To design a large Berry curvature, several approaches have been considered using nodal points and lines in momentum space[3–10]. Here we perform a high-throughput computational search and find that 25 percent doping of aluminium and gallium in alpha iron, a naturally abundant and low-cost element, dramatically enhances the ANE by a factor of more than ten, reaching about 4 and 6 microvolts per kelvin at room temperature, respectively, close to the highest value reported so far. The comparison between experiment and theory indicates that the Fermi energy tuning to the nodal web—a flat band structure made of interconnected nodal lines—is the key for the strong enhancement in the transverse thermoelectric coefficient, reaching a value of about 5 amperes per kelvin per metre with a logarithmic temperature dependence. We have also succeeded in fabricating thin films that exhibit a large ANE at zero field, which could be suitable for designing low-cost, flexible microelectronic thermoelectric generators[11–13].

Thermoelectricity, the conversion of heat current into electric energy, provides a key technology for versatile energy harvesting and for heat flow sensors. There is a rapidly growing demand for novel energy-harvesting technology to power Internet of Things sensors and wearable devices, particularly in the form of flexible, durable micro-thermoelectric generators (μ-TEGs). So far, the technology has relied on the longitudinal thermoelectric response known as the Seebeck effect[11–15]. Recently, its transverse counterpart in ferromagnets, the anomalous Nernst effect (ANE), has gained increasing attention, as it has a number of potential benefits[6–9,16–18]. For example, the transverse geometry of the Nernst effect enables efficient, large-area and flexible coverage of a curved heat source (Fig. 1a, left). It substantially reduces the number of production processes as well as the contact resistance of a thermopile, compared with a conventional thermoelectric device (Fig. 1a, right). In addition, the transverse geometry is hypothetically better suited for thermoelectric conversion as the Ettingshausen heat current should support the Nernst voltage, whereas the Peltier heat current may suppress the Seebeck voltage[18]. However, the ANE is too small compared with the Seebeck effect for any thermoelectric application. Thus, it is important to develop an approach to design a new class of materials that exhibit a large ANE at zero field. Moreover, as the use of rare and toxic elements would pose a barrier for applications, low-cost and safe elements should be used for thermoelectric materials.

Here we introduce two iron-based cubic compounds Fe_3X (where X is Ga or Al) as materials suitable for designing such low-cost, flexible μ-TEGs, in particular by using their thin-film forms. As detailed in Methods, our successful fabrication of their thin films enables us to obtain a large ANE of about 4 $\mu V\,K^{-1}$ for Fe_3Ga and about 2 $\mu V\,K^{-1}$ for Fe_3Al at room temperature using an in-plane temperature gradient (Extended Data Fig. 3a). In addition, our films of Fe_3Ga and Fe_3Al have in-plane magnetization with a coercivity B_c of about 40 Oe and 20 Oe, respectively, and exhibit a spontaneous ANE at zero field (Fig. 1c) for the out-of-plane temperature gradient. This enables us to design a much simpler μ-TEG than the conventional Seebeck analogues (Fig. 1a, Extended Data Fig. 4)[16]. Moreover, the specific power generation capacity $\Gamma_P = P_{max}/(A(\Delta T)^2)$ is estimated to be of the same order as or potentially greater than that of conventional μ-TEGs (Methods), where P_{max}, A and ΔT are the maximum power, the area of the thermopile device and the temperature difference, respectively[11–13]. In the following, we discuss

[1]Institute for Solid State Physics, University of Tokyo, Kashiwa, Japan. [2]Department of Physics, University of Tokyo, Tokyo, Japan. [3]CREST, Japan Science and Technology Agency (JST), Honcho Kawaguchi, Japan. [4]Nanomaterials Research Institute, Kanazawa University, Kanazawa, Japan. [5]Center for Emergent Matter Science (CEMS), RIKEN, Wako, Japan. [6]Department of Physics, Tohoku University, Sendai, Japan. [7]Department of Applied Physics, University of Tokyo, Tokyo, Japan. [8]Trans-scale Quantum Science Institute, University of Tokyo, Tokyo, Japan. [9]Institute for Quantum Matter and Department of Physics and Astronomy, Johns Hopkins University, Baltimore, MD, USA. [10]These authors contributed equally: Akito Sakai, Susumu Minami, Takashi Koretsune, Taishi Chen, Tomoya Higo. ✉e-mail: satoru@phys.s.u-tokyo.ac.jp

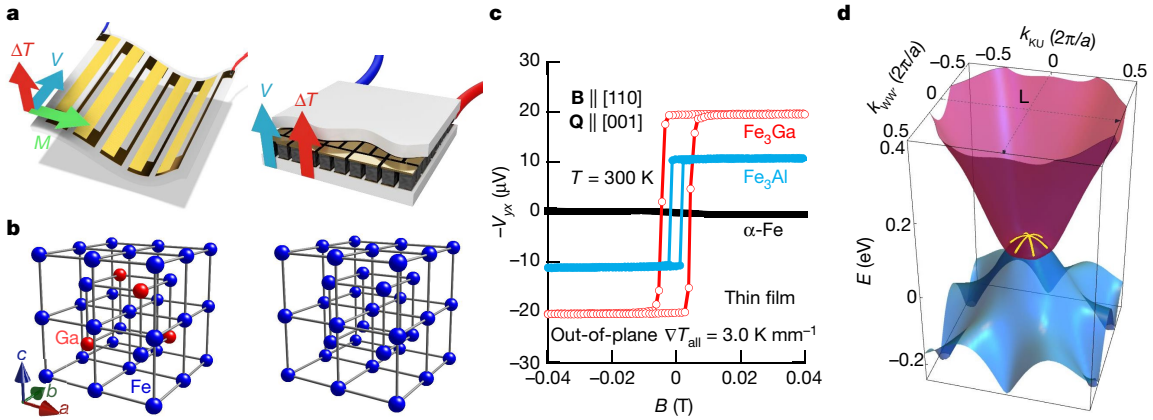

Fig. 1 | Transverse thermoelectric conversion, iron compounds and a nodal web. a, Thermopiles based on the ANE (left) and the Seebeck effect (right) have the transverse ($V \perp \Delta T$) and longitudinal ($V \parallel \Delta T$) geometries between the voltage (V) and temperature difference (ΔT), respectively. Compared with the pillar structure using p- and n-type semiconductors for the conventional thermoelectrics (right), the thermopile structure using the ANE may be as simple as, for example, a film type (yellow) deposited on a flexible substrate (left)[16]. M, magnetization. **b**, Crystal structures of Fe_3X (where X is Ga or Al) (left) and α-Fe (right). **c**, Magnetic field dependence of the Nernst voltage $-V_{yx}$ for the thin films of Fe_3Ga, Fe_3Al and α-Fe. As $-V_{yx}$ depends on the sample geometry and measurement conditions such as ΔT, we performed the measurements for all films with the same conditions (thickness, measurement set-up and so on). The temperature gradient in the sample (MgO substrate/Fe_3Ga, Fe_3Al or α-Fe/MgO), ∇T_{all}, is monitored to be 3.0 K mm^{-1}. The temperature gradient in the Fe_3Ga (Fe_3Al) layer is estimated to be $\nabla T \approx 0.86$ K mm^{-1} (1.0 K mm^{-1}) (Methods). **d**, Energy dispersion of the conduction band (red) and the valence band (blue) around the L point on the BZ boundary for Fe_3Ga. The nodal web is made of nodal lines, shown by the yellow lines (the same as in Fig. 4d), along which the flat portions of the conduction and the valence bands touch around the L point.

how we discovered these materials, their detailed physical properties using bulk single crystals and the origin of the large ANE.

Recent developments in the understanding of topological aspects in electronic transport led to the discovery of the large anomalous Hall and Nernst effects in spin liquids and antiferromagnetic metals[1,2,6,10,17,19–22]. It also fostered the finding that designing the electronic structure to locate the nodal points called Weyl points near the Fermi energy is crucial to enhance the Berry curvature and thus for ferromagnets to exhibit a large ANE beyond the conventional linear scaling law with magnetization[6–9]. The most popular ferromagnet is elemental alpha iron (α-Fe), which adopts a body-centred cubic (bcc) structure. Although its natural abundance is the highest among the magnetic elements, it does not exhibit a large ANE by itself[17] (Fig. 1c, Extended Data Fig. 3a). It would be useful for applications such as versatile energy harvesting and heat flow sensors if we could find a large ANE in iron-based compounds. To find candidate compounds efficiently, we used a high-throughput computational method to screen materials without synthesizing them first.

The inverse band-structure problem, namely identifying a material with given electronic properties, has a 20-year history[23]. Recently, triggered by the combination of advanced ab initio calculation methods and intelligent data-mining techniques for huge databases, in silico design has made great progress in a variety of fields in materials science[24–28]. However, high-throughput materials design for transport properties such as the ANE still remains a major challenge, as accurate calculation of not only one-particle quantities (such as the Kohn–Sham energy) but also two-particle quantities (such as the response function) is required. In addition, for the ANE, we need to calculate the Berry curvature using a sufficiently dense k-mesh in the three-dimensional (3D) Brillouin zone (BZ).

To reduce the formidable numerical cost for materials screening, we recently developed a code (a new version of pw2wannier in Quantum Espresso; Methods) that enables us to perform an efficient Wannier interpolation for calculations with relativistic ultrasoft pseudopotentials. We then performed a calculation for roughly 1,400 magnets available in the Materials Project[28] (Methods, Supplementary Table 1) to provide a comprehensive set of calculations for the transport properties of magnets. Among more than 250 iron-based compounds, we focused on binary compounds from the perspective of future applications. In Table 1, we list the five most promising candidates that would potentially exhibit a large ANE, with a transverse thermoelectric coefficient α_{yx} of more than 2.4 A K^{-1} m^{-1}. Here we select Fe_3Ga as a target material (Fig. 1b, Methods, Extended Data Figs. 1, 2), owing to its large $|\alpha_{yx}|$ and to its high Curie temperature $T_C \approx 720$ K (Table 1)[29–33]. In addition, its sister compound Fe_3Al ($T_C \approx 600$ K) is also of great interest fundamentally and technologically, as aluminium and iron are the most abundant metal elements in Earth's crust. Furthermore, as both compounds have the same cubic structure (Fig. 1b), we find all the properties to be nearly isotropic, which is convenient for application (Supplementary Information, Extended Data Figs. 6, 8, 9).

First, we present our experimental observation of the giant ANE in Fe_3Ga and Fe_3Al at room temperature. Figure 2a shows that the field dependence of the anomalous Nernst coefficient, S_{yx}, for Fe_3Ga and Fe_3Al saturates to a value as high as around 6 μV K^{-1} and around 4 μV K^{-1}, respectively, comparable to the value reported for Co_2MnGa (ref. [7]). This is striking as it indicates that 25% gallium doping leads to 20-fold enhancement in the ANE, compared with about 0.3 μV K^{-1} for α-Fe[17] (Fig. 2a), which shares the same bcc structure as Fe_3Ga and Fe_3Al (Fig. 1b). In addition, the Hall resistivity saturates to about 3 μΩ cm, one order magnitude larger than about 0.2 μΩ cm for α-Fe[17] (Fig. 2b). As shown in Fig. 2c, $-S_{yx}(T)$ exhibits a T-linear increase at low temperatures and saturation on heating above room temperature. The Hall resistivity also exhibits a systematic increase on heating for the entire range of temperatures (Fig. 2d).

In general, the anomalous Nernst coefficient is composed of two terms, that is, $S_{yx} = \alpha_{yx}\rho_{yy} - \sigma_{yx}\rho_{yy}S_{xx}$, where ρ_{yy} and σ_{yx} are the longitudinal resistivity and Hall conductivity, respectively (Supplementary Information, Extended Data Figs. 6, 7)[10]. Namely, the transverse charge flow comes from the transverse thermoelectric current $\alpha_{yx}(-\nabla T)$ and the Hall current. Figure 3a shows the temperature dependence of $-\alpha_{yx}(T)$. Fe_3Ga and Fe_3Al share a common feature: a nearly isotropic broad peak following the $T\ln T$ form, as we will discuss. It is also notable that $-\alpha_{yx}(T)$ in Fe_3Ga peaks at around 200 K, reaching around 5.2 A K^{-1} m^{-1}, the largest value for any magnetic compound. By contrast, the Hall conductivity is nearly T independent for both compounds, ranging between 350 and 600 Ω^{-1} cm^{-1} (Fig. 3b), the size of which is consistent with the scaling law with the longitudinal conductivity σ_{xx} for the intrinsic mechanism of the anomalous Hall effect (Supplementary Information, Extended

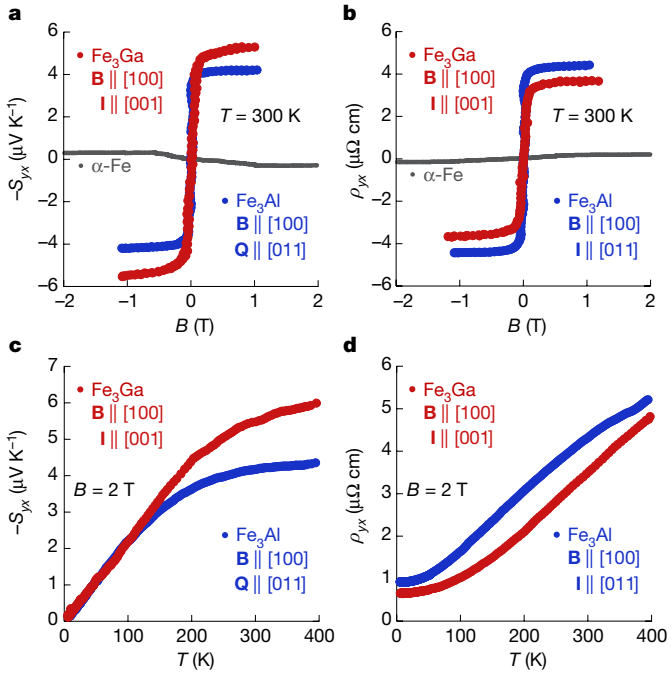

Fig. 2 | Large anomalous Nernst and Hall effects of Fe_3X. a, **b**, Magnetic field B dependence of the ANE $-S_{yx}$ (**a**) and the anomalous Hall effect ρ_{yx} (**b**) measured at room temperature. The magnitude of B in the horizontal axis is corrected for the demagnetization effect. The data for α-Fe are also plotted for comparison[17]. **c**, **d**, Temperature dependence of $-S_{yx}$ (**c**) and ρ_{yx} (**d**) measured under a magnetic field of 2 T along [100]. **B**, **Q** and **I** refer to the directions of the magnetic field, heat and electric currents, respectively.

Data Table 1)[1]. As a result, S_{yx} is dominated by the component $\alpha_{yx}(-\nabla T)$ for Fe_3Ga, as shown in Extended Data Fig. 7.

In ferromagnets, the Mott relation $\alpha_{yx} = -\frac{\pi^2}{3}\frac{k_B^2 T}{|e|}\left(\frac{\partial \sigma_{yx}}{\partial E}\right)_{E=E_F}$ (where k_B, e, E and E_F are the Boltzmann constant, elementary charge, energy and Fermi energy of the electrons, respectively) normally holds at $T \ll T_C$ and thus α_{yx} exhibits the Fermi liquid T-linear dependence. In fact, $-\alpha_{yx}/T$ shows a nearly T-constant behaviour at low temperatures for both Fe_3Ga and Fe_3Al (Fig. 3a, inset). To further examine the T dependence, in Fig. 3c we plot $g(T/T_m) \equiv (\alpha_{yx}/\alpha_{yx}(T_m))(T_m/T)$ versus T/T_m, where g is a normalized transverse thermoelectric coefficient and T_m refers to the temperature where $|\alpha_{yx}|$ attains its maximum (Extended Data Table 1). Interestingly, g for both Fe_3Ga and Fe_3Al shows a $\ln T$ dependence up to the highest temperature of our measurements, and shows saturation at large values below $T/T_m \approx 0.5$. Similarly, we also plot $\sigma_{yx}/\sigma_{yx}(T_m)$ for both compounds versus T/T_m and find that they roughly scale at $T/T_m > 0.5$ (Fig. 3d).

Using the Berry curvature expression for intrinsic σ_{yx} at $T = 0$ given by $\sigma_{yx}(E_F) = -(e^2/h)\sum_{n,\mathbf{k}} \Omega_{n,z}(\mathbf{k})\Theta(E_F - \varepsilon_{n,\mathbf{k}})$, the Mott relation can be rewritten as $\alpha_{yx} = \frac{\pi^2}{3}\frac{k_B^2 T}{|e|}\frac{e^2}{h}\sum_{n,\mathbf{k}} \Omega_{n,z}(\mathbf{k})\delta(E_F - \varepsilon_{n,\mathbf{k}})$, where the summation is taken for all the occupied states, $\Omega_{n,z}(\mathbf{k})$ is the Berry curvature along the $\hat{z}$ direction, n is the band index, $\Theta(\varepsilon)$ is the unit step function, $\delta(\varepsilon)$ is the Dirac delta function and h, $\mathbf{k}$ and $\varepsilon_{n,\mathbf{k}}$ are Planck's constant, the wavevector and the energy of the electrons in band n, respectively. Thus, it is essential to find the mechanism to simultaneously enhance the density of states and Berry curvature at the Fermi surfaces to obtain a large $-\alpha_{yx}/T$ as observed in Fe_3Ga and Fe_3Al. Using the Kubo formula, the Berry curvature can be described as $\Omega_{n,\mu\nu} = i\sum_{n' \neq n} \frac{\langle n | v_\mu | n' \rangle \langle n' | v_\nu | n \rangle}{(\varepsilon_n - \varepsilon_{n'})^2}$.

Here, $|n\rangle$ and ε_n are the cell-periodic Bloch eigenstates and eigenvalues, and v_μ and v_ν are velocity operators along directions μ and ν. The velocity operator is defined as $v_{\mu(\nu)} = \frac{\partial H(\mathbf{k})}{\partial k_{\mu(\nu)}}$, using the k-dependent Hamiltonian $H(\mathbf{k}) = e^{-i\mathbf{kr}} H e^{i\mathbf{kr}}$ where $\mathbf{r}$ is the position vector and H is the original Hamiltonian. This equation indicates that the Berry curvature would be strongly enhanced in the vicinity of the gapped line structure, which originally belongs to the nodal lines before introducing the spin–orbit coupling (SOC) (Fig. 1d). Moreover, the density of states (DOS) would be highly increased when the nodal lines are not only energy independent but also interconnected, forming a quasi-2D network. In the following, we show that such a 'nodal web' structure may arise when two nearly flat valence and conduction bands touch around a highly symmetric point (Figs. 1d, 4b–d) and eventually lead to a large Berry curvature on inclusion of SOC.

Table 1 | The five most promising iron-based binary compounds obtained from the high-throughput computation

Formula	Space group	α_{max} (A K^{-1} m^{-1})	T_c (K)
Fe_3Pt	$Pm\bar{3}m$	6.2	450
Fe_3Ga	$Fm\bar{3}m$	3.0	720
Fe_3Al	$Fm\bar{3}m$	2.7	600
Fe_3Si	$Fm\bar{3}m$	2.5	840
Fe_4N	$Pm\bar{3}m$	2.4	760

The compounds are sorted by the size of α_{max}, that is, the maximum value of α_{xy} estimated at the Fermi energy at $T \leq 500$ K. T_c is the experimentally obtained Curie temperature[29–33].

Figure 4a shows the band dispersion calculated using density functional theory (DFT) along highly symmetric lines in the momentum space. The numerically obtained σ_{yx} and $\partial\sigma_{yx}/\partial E$ exhibit a clear kink and an associated peak around 60 meV, respectively (Extended Data Fig. 5a, b). Correspondingly, we find that the temperature dependence of α_{yx}/T below about 200 K depends strongly on the energy E around 60 meV. In particular, α_{yx}/T exhibits the logarithmic temperature dependence over a wide T range at 62 meV (Extended Data Fig. 5c). Notably, using their own T_m (Extended Data Table 1), experiment and theory are in agreement when plotting $g = (\alpha_{yx}/\alpha_{yx}(T_m))(T_m/T)$ versus T/T_m (Fig. 3c). This indicates that the experimental results can be well reproduced by assuming that E is located at about $E_F = +74$ meV for Fe_3Ga and about $E_F = +86$ meV for Fe_3Al. Moreover, the reasonable agreement can be also found in the temperature dependence of the Hall conductivity by using the same set of parameters (Fig. 3d). In addition, theory indicates that the dominant band is made of minority-spin states and thus the upward shifts in E with respect to E_F can be naturally understood given that the magnetization is slightly overestimated in theory (Supplementary Information).

Figure 4b shows the 3D network made of the nodal lines calculated for Fe_3Ga without introducing SOC. All the nodal lines go through the whole BZ and are interconnected with each other, instead of forming a closed loop inside the BZ. In particular, we highlight the nodal-line network with a nearly flat energy dispersion at $E \approx +74$ meV as the nodal web (red and blue in Fig. 4b, c, yellow lines in Fig. 4d) around the L point. As two mirror eigenstates should be degenerate within each mirror plane (green shaded planes in Fig. 4d), the symmetry-protected six nodal lines branch off from another nodal line connecting the Γ and L points (Fig. 4c).

After introducing SOC, a gap opens along the nodal lines and induces the Berry curvature. We expect that the Berry curvature becomes substantially enhanced near the momenta that originally belong to the flat nodal web, such as the one around the L point. This is because along the nodal line, the gap between the two bands forming the nodal web should be small (Supplementary Information, Extended Data Fig. 5d–f) and, moreover, the flat energy dispersion must enhance the DOS associated with the Berry curvature.

To confirm this, we show the contour plot of the Berry curvature in Fig. 4e. The strongly enhanced Berry curvature is particularly seen at

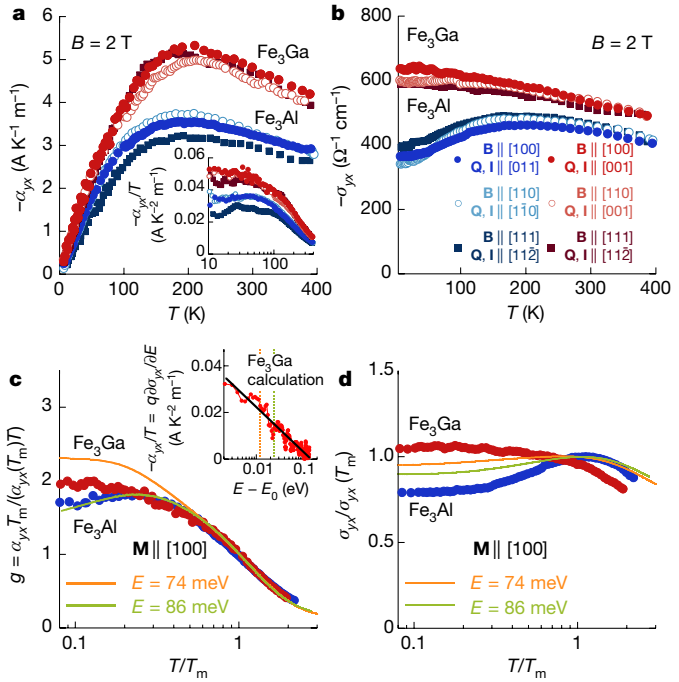

Fig. 3 | Giant transverse thermoelectric conductivity for Fe_3X. **a**, **b**, Temperature dependence of the transverse thermoelectric conductivity $-\alpha_{yx}$ (**a**) and the Hall conductivity $-\sigma_{yx}$ (**b**) obtained for various directions of **B**. In **b**, we define the data symbols for the combination of **Q** (**I**) and **B** directions for **a** and **b**. Both $-\alpha_{yx}$ and $-\sigma_{yx}$ exhibit nearly isotropic behaviours. The inset in **a** shows $-\alpha_{yx}/T$ versus T. **c**, **d**, Scaling relations of $-\alpha_{yx}$ (**c**) and σ_{yx} (**d**) versus T/T_m for **M** || [100]. Here, **M** and T_m refer to the magnetization and temperature at which $|\alpha_{yx}|$ attains its maximum (Extended Data Table 1). The solid lines are obtained from first-principles calculations at $E = +74$ meV (orange) and $E = +86$ meV (green). The inset in **c** shows the $-\ln|E - E_0|$ dependence (black solid line) of $\frac{\alpha_{yx}}{T} = -q\frac{\partial\sigma_{yx}}{\partial E}$ with $q = \frac{\pi^2 k_B^2}{3|e|}$ calculated in the vicinity of $E_0 = +62$ meV above the Fermi energy. The vertical broken lines indicate the characteristic energies $E = 74$ meV (orange) and $E = 86$ meV (green). Nearly isotropic character is found for **M** || [100], [110] and [111] (Supplementary Information, Extended Data Fig. 9).

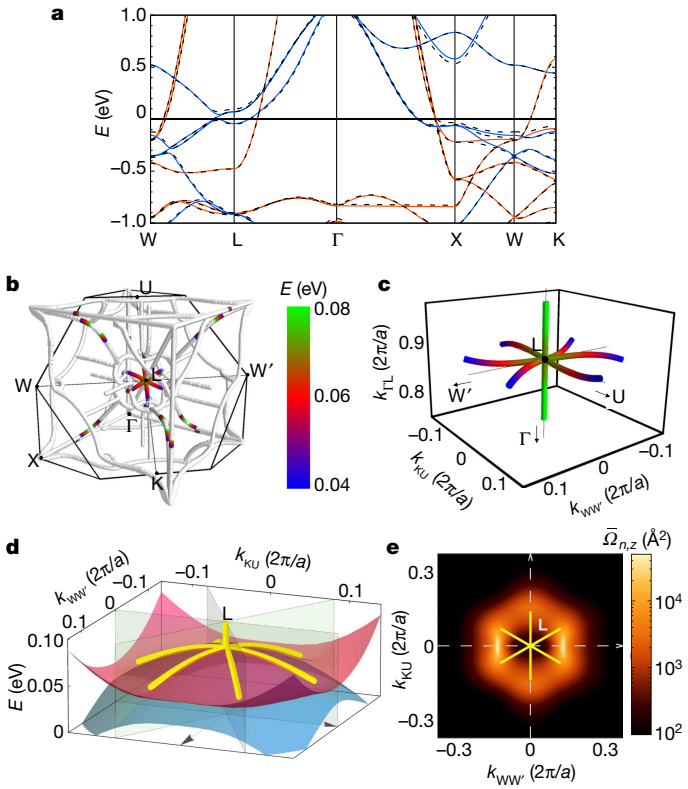

Fig. 4 | Evidence for the nodal web structure. **a**, Band structure around the Fermi energy. Red (blue) lines correspond to up (down) spin bands computed without SOC. Dashed lines show the bands calculated including SOC. **b**, BZ showing the nodal-line network. The nodal web formed around the L point is highlighted by the colour, which shows the energy dispersion of the nodal lines on a linear scale in a narrow range between 0.04 eV (blue) and 0.08 eV (green) above the Fermi energy. **c**, Three-dimensional network forming the nodal web around the L point. The $k_{WW'}$, k_{KU} and $k_{\Gamma L}$ axes indicate the directions parallel to W–W′, K–U and Γ–L, respectively. The nodal line (green) connecting the Γ and L points branches off into three nodal lines (red-blue) at the L point. **d**, Nearly flat energy dispersion of the nodal lines (yellow) forming the web structure around the L point, on the plane perpendicular to Γ–L. The $k_{WW'}$ and k_{KU} axes are the same as those in **c** and the z axis indicates the energy. A higher-energy (red) and a lower-energy (light blue) band touches with each other sharing gapless nodal lines (yellow lines, the same as in Fig. 1c) along the mirror planes (shaded green planes) in the case without SOC. **e**, Contour plot of the Berry curvature $\Omega_{n,z}$ of the lower-energy band n (in **d**) around the L point and nodal lines. The z direction is along [001] parallel to the magnetization. The Berry curvature was integrated within $[-\Delta k, \Delta k]$ along the $k_{\Gamma L}$ axis; $\bar{\Omega}_{n,z}(k_{WW'}, k_{KU}) = \int_{-\Delta k}^{\Delta k} dk_{\Gamma L}\Omega_{n,z}(k_{WW'}, k_{KU}, k_{\Gamma L})$. Δk was chosen to be sufficient to include the nodal web structure. The Berry curvature is strongly enhanced in the extended region around the nodal web structure (yellow lines) (Methods, Extended Data Fig. 5d–f).

the momenta connecting the edge of the nodal web around the L point on the BZ boundary, extending over a quasi-2D area spanned by the web. This situation could be comparable to the case of the band edge of the 1D system being accompanied by a logarithmic increase of the DOS as a function of energy. Similarly, $\partial\sigma_{yx}/\partial E$ exhibits a logarithmic energy dependence near $E = 62$ meV, indicating a divergent behaviour of the Berry curvature (Fig. 3c, inset). This leads to the $-\ln T$ dependence in α_{yx}/T found at 62 meV (Fig. 3c, Extended Data Fig. 5), the breakdown of the Mott relation. Such $-\ln T$ dependence has been previously discussed for the Lifshitz quantum critical point between type I and type II Weyl fermions found for Co_2MnGa (ref. [7]). Our scenario indicates that even without having Weyl points nearby, the formation of a flat nodal web may lead to the logarithmic enhancement of the transverse thermoelectric conductivity α_{yx}.

Our discovery of the large spontaneous transverse thermoelectric effects indicates that two iron-based compounds, Fe_3Ga and Fe_3Al, should be suitable for designing low-cost, flexible μ-TEGs by using their thin-film form. To gain a stable performance in daily use, it is important to enhance the coercivity further. Finally, it would be also an interesting future direction to look for an enhanced output by combining the ANE with the spin Seebeck effect, both of which occur in the same transverse geometry[34–37].

Note added in proof: During the review process of this paper, we became aware of a work by Nakayama et al.[38], the received date of which is one week later than ours. While they observed an enhancement in the ANE by gallium doping in bcc-Fe in its thin-film form, the materials used in their study are in a disordered phase, not the ordered $D0_3$ phase as studied in this work. Moreover, the maximum of $|S_{yx}|$ in Nakayama et al.[38] is less than half of the values found in our experiment and does not appear at $x = 0.25$ (that is, Fe_3Ga). As a result, the transverse thermoelectric conductivity α_{yx} is about five times smaller than our estimate, highlighting the importance of both the ordered $D0_3$ crystal structure and the stoichiometry of Fe_3Ga. Our work also contains the experimental results using not only thin films but also bulk single crystals over a wide temperature range with different field orientations. The combination of our comprehensive experimental observations and theoretical analysis have revealed that a 'nodal web' structure in the vicinity of the Fermi energy plays an important role in enhancing

the Berry curvature and thereby the transverse thermoelectric effect. In addition to the in-plane heat current configuration, we performed ANE measurements with the heat current applied perpendicular to the thin film, which reveals the zero-field spontaneous anomalous Nernst voltage with a coercivity of about 40 Oe in Fe_3Ga.

Online content

Any methods, additional references, Nature Research reporting summaries, source data, extended data, supplementary information, acknowledgements, peer review information; details of author contributions and competing interests; and statements of data and code availability are available at https://doi.org/10.1038/s41586-020-2230-z.

1. Nagaosa, N., Sinova, J., Onoda, S., MacDonald, A. H. & Ong, N. P. Anomalous Hall effect. *Rev. Mod. Phys.* **82**, 1539–1592 (2010).
2. Xiao, D., Chang, M.-C. & Niu, Q. Berry phase effects on electronic properties. *Rev. Mod. Phys*. **82**, 1959–2007 (2010).
3. Wan, X., Turner, A. M., Vishwanath, A. & Savrasov, S. Y. Topological semimetal and Fermi arc surface states in the electronic structure of pyrochlore iridates. *Phys. Rev. B* **83**, 205101 (2011).
4. Burkov, A. A. & Balents, L. Weyl semimetal in a topological insulator multilayer. *Phys. Rev. Lett*. **107**, 127205 (2011).
5. Fang, C., Chen, Y., Kee, H.-Y. & Fu, L. Topological nodal line semimetals with and without spin-orbital coupling. *Phys. Rev. B* **92**, 081201 (2015).
6. Ikhlas, M. et al. Large anomalous Nernst effect at room temperature in a chiral antiferromagnet. *Nat. Phys*. **13**, 1085–1090 (2017).
7. Sakai, A. et al. Giant anomalous Nernst effect and quantum-critical scaling in a ferromagnetic semimetal. *Nat. Phys*. **14**, 1119–1124 (2018).
8. Noky, J., Xu, Q., Felser, C. & Sun, Y. Large anomalous Hall and Nernst effects from nodal line symmetry breaking in Fe_2MnX (X = P, As, Sb). *Phys. Rev. B* **99**, 165117 (2019).
9. Guin, S. N. et al. Zero-field Nernst effect in a ferromagnetic kagome-lattice Weyl-semimetal $Co_3Sn_2S_2$. *Adv. Mater*. **31**, 1806622 (2019).
10. Lee, W.-L., Watauchi, S., Miller, V. L., Cava, R. J. & Ong, N. P. Anomalous Hall heat current and Nernst effect in the $CuCr_2Se_{4-x}Br_x$ ferromagnet. *Phys. Rev. Lett*. **93**, 226601 (2004).
11. Bottner, H., Nurnus, J., Schubert, A. & Volkert, F. New high density micro structured thermogenerators for stand alone sensor systems. In *Proc. 26th Int. Conf. Thermoelectrics* 306–309 (IEEE, 2007).
12. Glatz, W., Schwyter, E., Durrer, L. & Hierold, C. Bi_2Te_3-based flexible micro thermoelectric generator with optimized design. *J. Microelectromech. Syst*. **18**, 763–772 (2009).
13. Hu, G., Edwards, H. & Lee, M. Silicon integrated circuit thermoelectric generators with a high specific power generation capacity. *Nat. Electron*. **2**, 300–306 (2019).
14. Bell, L. E. Cooling, heating, generating power, and recovering waste heat with thermoelectric systems. *Science* **321**, 1457–1461 (2008).
15. Snyder, G. J. & Toberer, E. S. Complex thermoelectric materials. *Nat. Mater*. **7**, 105–114 (2008).
16. Sakuraba, Y. et al. Anomalous Nernst effect in $L1_0$-FePt/MnGa thermopiles for new thermoelectric applications. *Appl. Phys. Express* **6**, 033003 (2013).
17. Li, X. et al. Anomalous Nernst and Righi-Leduc effects in Mn_3Sn: Berry curvature and entropy flow. *Phys. Rev. Lett*. **119**, 056601 (2017).
18. Mizuguchi, M. & Nakatsuji, S. Energy-harvesting materials based on the anomalous Nernst effect. *Sci. Technol. Adv. Mater*. **20**, 262–275 (2019).
19. Machida, Y., Nakatsuji, S., Onoda, S., Tayama, T. & Sakakibara, T. Time-reversal symmetry breaking and spontaneous Hall effect without magnetic dipole order. *Nature* **463**, 210–213 (2010).
20. Nakatsuji, S., Kiyohara, N. & Higo, T. Large anomalous Hall effect in a noncollinear antiferromagnet at room temperature. *Nature* **527**, 212–215 (2015).
21. Kiyohara, N., Tomita, T. & Nakatsuji, S. Giant anomalous Hall effect in the chiral antiferromagnet Mn_3Ge. *Phys. Rev. Appl*. **5**, 064009 (2016).
22. Nayak, A. K. et al. Large anomalous Hall effect driven by a nonvanishing Berry curvature in the noncolinear antiferromagnet Mn_3Ge. *Sci. Adv*. **2**, e1501870 (2016).
23. Franceschetti, A. & Zunger, A. The inverse band-structure problem of finding an atomic configuration with given electronic properties. *Nature* **402**, 60–63 (1999).
24. Mounet, N. et al. Two-dimensional materials from high-throughput computational exfoliation of experimentally known compounds. *Nat. Nanotechnol*. **13**, 246–252 (2018).
25. Curtarolo, S. et al. The high-throughput highway to computational materials design. *Nat. Mater*. **12**, 191–201 (2013).
26. Saal, J. E., Kirklin, S., Aykol, M., Meredig, B. & Wolverton, C. Materials design and discovery with high-throughput density functional theory: the open quantum materials database (OQMD). *JOM* **65**, 1501–1509 (2013).
27. Curtarolo, S. et al. AFLOW: an automatic framework for high-throughput materials discovery. *Comput. Mater. Sci*. **58**, 218–226 (2012).
28. Jain, A. et al. A high-throughput infrastructure for density functional theory calculations. *Comput. Mater. Sci*. **50**, 2295–2310 (2011).
29. Sumiyama, K., Emoto, Y., Shiga, M. & Nakamura, Y. Magnetic and magnetovolume properties of the Cu_3Au type ordered Fe-Pt alloys around the γ-α phase boundary. *J. Phys. Soc. Jpn* **50**, 3296–3302 (1981).
30. Kawamiya, N., Adachi, K. & Nakamura, Y. Magnetic properties and Mössbauer investigations of Fe-Ga alloys. *J. Phys. Soc. Jpn* **33**, 1318–1327 (1972).
31. Shinohara, T. The effect of atomic ordering on the magnetic properties of Fe-Al alloys. *J. Phys. Soc. Jpn* **19**, 51–58 (1964).
32. Niculescu, V. et al. Relating structural, magnetization, and hyperfine field studies to a local environment model in $Fe_{3-x}V_xSi$ and $Fe_{3-x}Mn_xSi$. *Phys. Rev. B* **14**, 4160–4176 (1976).
33. Guilland, C. & Creveaux, H. Preparation and magnetic properties of the compound Fe_4N. *Compt. Rend. Acad. Sci*. **222**, 1170–1173 (1946).
34. Uchida, K. et al. Observation of the spin Seebeck effect. *Nature* **455**, 778–781 (2008).
35. Ramos, R. et al. Observation of the spin Seebeck effect in epitaxial Fe_3O_4 thin films. *Appl. Phys. Lett*. **102**, 072413 (2013).
36. Boona, S. R., Vandaele, K., Boona, I. N., McComb, D. W. & Heremans, J. P. Observation of spin Seebeck contribution to the transverse thermopower in Ni-Pt and MnBi-Au bulk nanocomposites. *Nat. Commun*. **7**, 13714 (2016).
37. Kannan, H., Fan, X., Celik, H., Han, X. & Xiao, J. Q. Thickness dependence of anomalous Nernst coefficient and longitudinal spin Seebeck effect in ferromagnetic Ni_xFe_{100-x} films. *Sci. Rep*. **7**, 6175 (2017).
38. Nakayama, H. et al. Mechanism of strong enhancement of anomalous Nernst effect in Fe by Ga substitution. *Phys. Rev. Mater*. **3**, 114412 (2019).

Methods

Single-crystal growth and experimental methods

Single crystals of Fe_3X (where X is Ga or Al) were prepared by the Czochralski method after making polycrystalline samples by arc melting. As-grown single crystals were used for all the measurements. Our analyses using both inductively coupled plasma spectroscopy and energy dispersive X-ray analysis indicate that our single crystals are stoichiometric within a few percent resolution. The samples were oriented by the Laue backscattering method and subsequently cut by spark erosion. The bar-shaped sample with flat polished surfaces was used for all the transport measurements, including the electric resistivity and Hall, Seebeck and Nernst effects in a commercial system (thermal transport option (TTO) of physical property measurement system (PPMS), Quantum Design). A schematic of the measurement setup is provided in Extended Data Fig. 3b. The three gold-plated copper leads were attached to the sides of a rectangular parallelepiped sample with silver epoxy, which were connected to one resistive heater and two (hot and cold) Cernox1050 thermometers by screws. Two copper wires were also attached on the side surfaces of the sample with silver epoxy, which were used to measure the Hall and Nernst voltages. One of the edges of the sample was directly clamped to the heat sink of the TTO puck by the screw. The magnetic field **B** was applied along [100], [110] or [111]. The electric (thermal) current **I** (**Q**) was applied perpendicular to **B**, namely **I** (**Q**) || [001] or [011] for **B** || [100], [001] or [1$\bar{1}$0] for **B** || [110], and [11$\bar{2}$] for **I** (**Q**) || [111] without a transverse component (adiabatic Nernst effect). All the transport properties represent steady-state values, which were taken under a constant heat/electric current. Magnetization was measured by using a commercial SQUID magnetometer (MPMS, Quantum Design) after reshaping the single crystal into a tiny piece (about 0.1 mg). During the measurement, the magnetic field was fixed at each measurement point in the persistent mode.

The anisotropy in the Nernst and Hall effects and magnetization was found to be small, as we discuss in Supplementary Information (Extended Data Figs. 6, 8, 9).

Crystal structure

Fe_3X has a bcc derivative structure, namely, an ordered $D0_3$ structure ($Fm\bar{3}m$), partially ordered B_2 structure ($Pm\bar{3}m$), which corresponds to stoichiometric Fe_3X phase, and fully disordered A_2 structure ($Im\bar{3}m$). Our single crystals were confirmed to have a $D0_3$ structure by X-ray diffraction (XRD) (Extended Data Fig. 1a, b) and selected area electron diffraction (Extended Data Fig. 1c). The XRD pattern is well reproduced by the Rietveld analysis as shown by the solid line in Extended Data Fig. 1a, b, indicating the single phase of the $D0_3$ Fe_3X with a lattice constant of $a = 5.80$ Å for Fe_3Ga and $a = 5.79$ Å for Fe_3Al. For Fe_3Al, (111) peak is clearly observed around $2\theta \approx 27°$ (where 2θ is the angle between incident and diffracted X-ray beam directions), indicating the $D0_3$ ordered structure. For Fe_3Ga, the (111) peak is expected to be very small (about 0.8% of the (220) peak) and cannot be observed in our experiment. Nevertheless, we detect the signal from (111) by the electron diffraction as shown in Extended Data Fig. 1c. While the (111) and (200) reflections are detected by a charge-coupled device camera for Fe_3Al, they are detected by only an imaging plate with long exposure time for Fe_3Ga. Note that the effect of multiple reflection and diffraction from the oxide appears due to the high sensitivity of the imaging plate and long exposure time. For the powder XRD measurements, we annealed the sample at 630 °C for about 10 h for Fe_3Ga, and 400 °C for about 20 h for Fe_3Al after making powder from single crystals to remove the strains and distortions introduced by the crushing procedure.

Fabrication and characterization for Fe_3Al and Fe_3Ga thin films

Fe_3Al films were fabricated on MgO(001) substrates by a molecular beam epitaxy method under ultrahigh vacuum (UHV). The base pressure of the UHV chamber was below 2×10^{-8} Pa. Before the deposition, the substrates were annealed at 800 °C for 10 min in the UHV chamber. An MgO layer (5 nm) was deposited at a rate of 0.1 Å s^{-1} at room temperature on the MgO substrate as a seed layer for the Fe_3Al layer. The Fe_3Al layer (50 nm) was deposited at a rate of 0.2 Å s^{-1} at room temperature and subsequently it was annealed at 450 °C for 30 min.

Fe_3Ga films were fabricated on MgO(001) substrates by a d.c. magnetron sputtering method. The base pressure of the chamber was below 5×10^{-7} Pa. Before the deposition, the substrates were annealed at 800 °C for 10 min in the chamber. An Fe_3Ga layer (50 nm) was deposited at a rate of 0.4 Å s^{-1} at room temperature and subsequently it was annealed at 500 °C for 30 min.

The compositions of the Fe_3Al and Fe_3Ga layers were estimated to be $Fe_{2.7}Al_{1.3}$ and $Fe_{3.07}Ga_{0.93}$, respectively, by scanning electron microscopy-energy dispersive X-ray spectroscopy. To prevent oxidation, the Fe_3Al and Fe_3Ga layers were both capped with MgO (5 nm) under the same conditions as described for the seed layer.

The structural properties of the Fe_3Al and Fe_3Ga films were analysed by XRD measurements using a Cu-Kα source. Extended Data Fig. 2a shows the XRD patterns ($2\theta/\omega$-scan) of the Fe_3Al and Fe_3Ga films made by the solid phase epitaxy. We confirmed the (002) and (004) peaks in the Fe_3Al and Fe_3Ga films indexed by the Bravais lattice of the bcc structure with the lattice constants of $c = 5.71$ Å and $c = 5.74$ Å, respectively. Extended Data Fig. 2b presents the XRD patterns (φ-scan) of the {202} planes of the Fe_3Al and Fe_3Ga films, and the MgO substrate. The reflections of both Fe_3Al and Fe_3Ga films show fourfold symmetry with 90° intervals. These XRD patterns indicate that these layers are grown epitaxially with a well-defined in-plane orientation. As the peaks of Fe_3X {202} are shifted by 45° with respect to the corresponding {202} peaks of MgO, the crystallographic relationship is determined to be $Fe_3X(001)[110]||MgO(001)[100]$. The presence of the superlattice (111) peak was further examined to determine whether the films are chemically ordered in the $D0_3$ type. Extended Data Fig. 2c shows the (111) peaks in the XRD pattern ($2\theta/\omega$-scan) for the Fe_3Al and Fe_3Ga thin films, indicating the $D0_3$ structure.

Magneto-thermoelectric transport properties of Fe_3Al and Fe_3Ga thin films

To estimate the anomalous Nernst coefficient S_{yx} of the Fe_3Ga and Fe_3Al thin films, we performed the Nernst voltage measurements with the temperature gradient ∇T along both the in-plane and the out-of-plane directions. For the measurements using the former 'in-plane' ∇T configuration, we employed the same apparatus (TTO of PPMS) and the same temperature gradient configuration as used to measure the bulk Fe_3Ga and Fe_3Al samples (see 'Single-crystal growth and experimental methods' and Extended Data Fig. 3b). Note that ∇T in the thin film is determined by the ∇T in the substrate for the 'in-plane' ∇T configuration, as the thermal resistance of the sample (MgO substrate (500 μm)/Fe_3X (50 nm)/MgO capping layer (5 nm)) is dominated by the MgO substrate as follows. The total thermal resistance θ_{total} is described as $1/\theta_{total} = 1/\theta_{substrate} + 1/\theta_{Fe_3X} + 1/\theta_{cap}$, where $\theta_{substrate}$, θ_{Fe_3X} and θ_{cap} are the thermal resistance of the MgO substrate including the seed layer, Fe_3X (50 nm) and MgO capping layer, respectively. Each thermal resistance can be estimated by using the sample dimensions as described in Extended Data Fig. 3b as well as the thermal conductivity of MgO and Fe_3X, $\kappa_{MgO} \approx 60$ W K^{-1} m^{-1} and $\kappa_{Fe_3X} \approx 20$ W K^{-1} m^{-1} (refs. [39,40]). As $\theta_{substrate} \approx 150$ K W^{-1} is much smaller than both $\theta_{Fe_3X} \approx 4.5 \times 10^6$ K W^{-1} and $\theta_{cap} \approx 1.5 \times 10^7$ K W^{-1}, $1/\theta_{Fe_3X}$ and $1/\theta_{cap}$ are negligibly small and thus we do not need to consider any contributions other than the one from the MgO substrate to estimate the in-plane temperature gradient of the sample. Independently, we carried out the thermal conductivity measurement of the same sample and confirmed that the thermal conductivity is estimated to be 56 W K^{-1} m^{-1}, which is consistent with the above estimate based on literature[39].

Extended Data Fig. 3a shows the field dependence of the anomalous Nernst coefficient for the in-plane temperature gradient ∇T (heat

current $\mathbf{Q} \parallel [1\bar{1}0]$) and the perpendicular magnetic field ($\mathbf{B} \parallel [001]$) at 300 K. The Nernst coefficient is estimated to be $|S_{yx}| = 4.0\ \mu V\ K^{-1}$, $1.8\ \mu V\ K^{-1}$ and $0.3\ \mu V\ K^{-1}$ for the Fe_3Ga, Fe_3Al and α-Fe (50 nm) thin films, respectively, consistent with the bulk results. Note that the α-Fe (50 nm) film was epitaxially grown by the molecular beam epitaxy method on the MgO(001) substrate with the same in-plane orientation as the Fe_3X films, and the linear-in-B ordinary Nernst effect $N \approx -0.05\ \mu V\ KT^{-1}$ is subtracted for the α-Fe sample.

In addition to the abovementioned 'in-plane' ∇T and out-of-plane $\mathbf{B}$ configuration, we performed the Nernst effect measurements with 'out-of-plane' ∇T and in-plane $\mathbf{B}$, which is a more practical configuration for the magneto-thermoelectric devices.

The films used for the 'out-of-plane' ∇T measurements are sandwiched from top to bottom, in the following order, as illustrated in Extended Data Fig. 3c: [(1) Resistive heater] + [(2) Copper heat sink] + [(3) Thermal interface silicone soft pad (TIP) (500 μm)] + [(4) MgO capping layer (5 nm)] + [(5) Sample: Fe_3Ga, Fe_3Al or α-Fe (50 nm)] + [(6) MgO substrate (500 μm)] + [(7) TIP (500 μm)] + [(8) Copper heat sink]. Here we used a thermal interface silicone pad TC-50HSV-1.4 (thermal conductivity, $\kappa \approx 1.3\ W\ K^{-1}\ m^{-1}$; thermal resistance, about $1.1\ K\ W^{-1}$; Shin-Etsu Silicone) for both TIP layers. In the measurements, the magnetic field and heat current were respectively applied to [110] and [001] directions of each film. As the stacking structure is complicated, it is important to make further confirmations of the Nernst effects using several independent methods to estimate the temperature gradient/difference.

Figure 1c shows the field dependence of the Nernst voltage of the Fe_3X and α-Fe thin films at room temperature. ΔT_{all} is monitored to be 1.5 K in all the samples by two calibrated thermocouples placed on the top and bottom surfaces of the samples (Extended Data Fig. 3c). The Fe_3Ga (Fe_3Al) sample shows a sharp hysteresis with a zero-field value of 19.8 μV (10.6 μV) and coercivity of 40 Oe (20 Oe). These signals are much larger than those obtained for α-Fe. An isotropic character of the anomalous Nernst coefficient, as confirmed in the bulk Fe_3X measurements (Supplementary Information, Extended Data Fig. 8), allows us to adopt the in-plane Nernst coefficient (Extended Data Fig. 3a) to estimate the applied out-of-plane temperature difference. The temperature difference and temperature gradient of the Fe_3Ga (Fe_3Al) layer are estimated to be about 4.5×10^{-5} K and 0.9 K mm^{-1} (5.4×10^{-5} K and 1.1 K mm^{-1}), respectively. These values are consistent with the temperature difference and gradient estimated by another independent method, as we will discuss below.

To estimate the temperature difference and gradient applied in the Fe_3X film (50 nm), the Nernst effect of an α-Fe epitaxial thin film (50 nm) was measured under the same conditions as in the case of the Fe_3Al film. By assuming that the α-Fe film has the same anomalous Nernst coefficient S_{yx} and thermal conductivity as those reported for the bulk α-Fe ($S_{yx,\alpha\text{-Fe}} = 0.3\ \mu V\ K^{-1}$ (ref. [17]) and $\kappa_{\alpha\text{-Fe}} = 80\ W\ K^{-1}\ m^{-1}$ (ref. [41])), the temperature gradient, temperature difference and heat flux of the α-Fe film (50 nm) can be estimated to be $\nabla T_{\alpha\text{-Fe}} = 0.19$ K mm^{-1}, $\Delta T_{\alpha\text{-Fe}} = 1.0 \times 10^{-5}$ K and $Q_{\alpha\text{-Fe}} \approx 0.21$ W, respectively.

As we use the same stacking sequence and temperature gradient (difference) for both α-Fe and Fe_3X on MgO (that is, $\nabla T_{all} = 3.0$ K mm^{-1}, $\Delta T_{all} = 1.5$ K), the heat current of Fe_3X is expected to be almost the same, that is, $Q_{Fe_3X} \approx 0.21$ W. By using the thermal conductivity κ_{Fe_3Ga} (κ_{Fe_3Al}) = 19.0 (17.4) $W\ K^{-1}\ m^{-1}$ of Fe_3X presented in Extended Data Fig. 6 (Supplementary Information), the temperature gradient and temperature difference applied in the Fe_3Ga (Fe_3Al) film can be estimated to be $\nabla T_{Fe_3Ga} = 0.82$ K mm^{-1} and $\Delta T_{Fe_3Ga} = 4.1 \times 10^{-5}$ K ($\nabla T_{Fe_3Al} = 0.89$ K mm^{-1} and $\Delta T_{Fe_3Al} = 4.5 \times 10^{-5}$ K), respectively. These are nearly the same values as those calculated using the Nernst voltage (Fig. 1c) and the Nernst coefficients obtained in the 'in-plane' ∇T configuration (Extended Data Fig. 3a), indicating that our method to estimate the temperature gradient is reasonable. Another way of confirming the validity for the 'out-of-plane' ∇T measurement is to examine the Nernst coefficients using the above estimates of the temperature difference and the Nernst voltage. The obtained Nernst coefficients are estimated to be $S_{yx} = 4.4\ \mu V\ K^{-1}$ and $2.2\ \mu V\ K^{-1}$ for the Fe_3Ga and Fe_3Al 50-nm thin films, respectively, which are nearly the same values as those found using the Nernst effect measurements in the 'in-plane' ∇T configuration (Extended Data Fig. 3a).

Estimation of the specific power generation capacity $\Gamma_P = P_{max}/(A(\Delta T)^2)$

In this section, we evaluate how much power can be obtained from the μ-TEG using the anomalous Nernst effect of Fe_3X. Extended Data Fig. 4 shows a schematic of the μ-TEG based on the anomalous Nernst effect[16]. The thermopile consists of an alternating array of the Fe_3X (yellow) and electrode (gold) wires placed on a substrate. Two-hundred wires, whose thickness, width and length are designed to be $t = 1$ μm, $w = 20$ μm and $l = 9$ mm, respectively, are aligned in the substrate with the area of $A = 1\ cm^2$. Owing to the lateral configuration of the anomalous Nernst effect, a temperature difference ΔT is applied perpendicular to the plane and the resultant voltage is $V/\Delta T = LS_{yx}/t = 200lS_{yx}/t = 10.8\ V\ K^{-1}$ for Fe_3Ga ($S_{yx} \approx 6\ \mu V\ K^{-1}$) and $7.2\ V\ K^{-1}$ for Fe_3Al ($S_{yx} \approx 4\ \mu V\ K^{-1}$), where L is the total length of the material. Note that this 'geometrically enhanced' Nernst voltage is comparable to the μ-TEG output for the 25,000 p–n pairs of Bi_2Te_3. For practical applications, the main concern is not widely used efficiency or figure of merit ZT, but specific power generation capacity $\Gamma_P = P_{max}/(A(\Delta T)^2)$, which indicates how much power is generated from a temperature difference ΔT (refs. [11–13]). Γ_P for our μ-TEG design is estimated to be $\Gamma_P = Lw{S_{yx}}^2/(4t\rho)/(1\ cm^2) = 324\ \mu W\ (K^2\ cm^2)^{-1}$ for Fe_3Ga and $144\ \mu W\ (K^2\ cm^2)^{-1}$ for Fe_3Al. The values estimated here are the hypothetical upper limit. Although the actual values may be reduced by a factor of about ten in a practical μ-TEG, they would be still comparable to or higher than those reported for conventional μ-TEGs to date[11–13].

High-throughput calculation of thermoelectric conductivity

For the crystal structures in the Materials Project[28], the electronic structures were calculated within the generalized gradient approximation using the Quantum Espresso code[42]. The crystal structure was analysed using cif2cell[43] and ultrasoft pseudopotentials in the PSLibrary[44] were used. The magnetic moment was assumed along the z axis and the SOCs were included. Wannier interpolation was automatically performed by using the wannier90 code[45] with the appropriate initial orbitals and energy ranges; that is, the atomic orbitals whose energy level is higher than −1 Rydberg (Ry) were selected as initial orbitals and the Kohn–Sham orbitals with the energy range below E_F of +1 eV were fully used to construct the Wannier orbitals. The script used for this calculation is available at https://github.com/wannier-utils-dev/cif2qewan/. For each Wannier interpolated Hamiltonian, we confirmed that the energy difference between the interpolated band and the original DFT band is less than 0.2 eV. In terms of the computational cost, we limited the number of atoms in the unit cell to be less than eight atoms. With this criterion, the number of successfully obtained Wannier Hamiltonians is 1,419, including 265 iron-based compounds. The list of α_{yx} calculated for all the 1,419 compounds are shown in Supplementary Table 1.

For all these Wannier Hamiltonians, the intrinsic contribution of the anomalous Hall conductivity σ_{xy} and the anomalous transverse thermoelectric conductivity α_{xy} were calculated through the Berry curvature formula as

$$\sigma_{xy}(T,\mu) = -\frac{e^2}{\hbar}\int \frac{d\mathbf{k}}{(2\pi)^3}\Omega_{n,z}(\mathbf{k})f_{n,\mathbf{k}} \quad (1)$$

$$\alpha_{xy}(T,\mu) = -\frac{1}{e}\int d\varepsilon\left(-\frac{\partial f}{\partial \varepsilon}\right)\sigma_{xy}(0,\varepsilon)\frac{\varepsilon-\mu}{T} \quad (2)$$

where e, $\hbar$, ε, f, μ and $\Omega_{n,z}$ are the elementary charge with a negative sign, the reduced Planck constant, the band energy, the Fermi–Dirac

distribution function with the band index n and the wavevector $\mathbf{k}$, the chemical potential and the z component of the Berry curvature, respectively.

To select the candidates, we first sorted the list by the magnitude of α_{max}, which refers to the maximum value of $|\alpha_{yx}|$ estimated at the Fermi energy below 500 K. Then, we focused on the iron-based compounds as iron is the least expensive element. Finally, we removed paramagnets, antiferromagnets and the materials that do not exist in past experimental reports.

DFT calculation

The electronic structures of Fe_3X were obtained by using the OpenMX code[46], where the exchange-correlation functional within the generalized-gradient approximation and norm-conserving pseudopotentials[47] were employed. The spin–orbit interaction was included by using total angular momentum-dependent pseudopotentials[48]. The wave functions were expanded by a linear combination of multiple pseudoatomic orbitals[49]. A set of pseudoatomic orbital basis was specified as Fe6.0-*s*3*p*3*d*3, Al7.0-*s*3*p*3*d*1 and Ga7.0-*s*3*p*3*d*3, where the number after each element stands for the radial cutoff in the unit of Bohr and the integer after *s*, *p* and *d* indicates the radial multiplicity of each angular momentum component. The cutoff energies for a charge density of 800.0 Ry and a *k*-point mesh of 35 × 35 × 35 were used. The lattice constants of Fe_3Ga and Fe_3Al were set to 5.80 Å and 5.79 Å, respectively[50,51]. The evaluated magnetic moments of Fe_3Ga and Fe_3Al are 6.69 Bohr magneton per formula unit (μ_B f.u.$^{-1}$) and 5.93 μ_B f.u.$^{-1}$, respectively, which are close to the experimentally obtained values and consistent with previously calculated results[52,53]. The nodal lines were obtained by monitoring the degeneracy of eigenvalues in the momentum space based on the electronic structure without SOC.

Wannier representation and transport properties

From the Bloch states obtained in the DFT calculation described above, a Wannier basis set was constructed by using the wannier90 code[45]. The basis was composed of *d*-character orbitals localized at each Fe site, (*s*,*p*)-character ones at the Al sites and *p*-character ones at the Ga sites, that is, 38 orbitals per f.u. of Fe_3Al and 36 orbitals per f.u. of Fe_3Ga in total, including the spin multiplicity. These sets were constructed from the Bloch functions in the energy window ranging from −15 eV to 50 eV, which include 92 bands for Fe_3Al and 110 bands for Fe_3Ga.

The anomalous Hall conductivity σ_{xy} and the anomalous transverse thermoelectric conductivity α_{xy} that intrinsically appear in crystalline systems can be expressed with the out-of-plane component $\Omega_{n,z}(\mathbf{k})$ of the Berry curvature as described in equations (1) and (2). σ_{xy} and α_{xy} shown in Fig. 3c, d were calculated according to the above equations in the Wannier representation. For the numerical integration, a *k*-point mesh of 100 × 100 × 100 and in addition an adaptive mesh of $N_{adp} = 3 \times 3 \times 3$ in regions with large $\Omega_{n,z}$ were used. This adaptive mesh is already sufficiently large as we confirmed that the relative change of $-\sigma_{yx}$ calculated with $N_{adp} = 3 \times 3 \times 3$ and $6 \times 6 \times 6$ is less than 1%.

Extended Data Fig. 5a, b shows the energy dependence of the Hall conductivity $-\sigma_{yx}$ and the transverse thermoelectric conductivity estimated using the Mott relation, namely $\alpha_{yx}/T = -q(\partial\sigma_{yx}/\partial E)_{E=E_F}$ with $q = \frac{\pi^2}{3}\frac{k_B^2}{|e|}$. Extended Data Fig. 5c shows the temperature dependence of $-\alpha_{yx}/T$ calculated using equation (2) for various energies.

Data availability

The data that support the plots within this paper and the other findings of this study are available from the corresponding author upon reasonable request.

39. Slack, G. A. Thermal conductivity of MgO, Al_2O_3, $MgAl_2O_4$, and Fe_3O_4 crystals from 3° to 300° K. *Phys. Rev.* **126**, 427–441 (1962).
40. Rudajevová, A. & Buriánek, J. Determination of thermal diffusivity and thermal conductivity of Fe-Al alloys in the concentration range 22 to 50 at.% Al. *J. Phase Equilibria* **22**, 560–563 (2001).
41. Gaviot, E. et al. Distribution-patterned radiometers: a new paradigm for irradiance measurement. *Proc. SPIE* **3061**, 800–810 (1997).
42. Giannozzi, P. et al. QUANTUM ESPRESSO: a modular and open-source software project for quantum simulations of materials. *J. Phys. Condens. Matter* **21**, 395502 (2009).
43. Björkman, T. CIF2Cell: generating geometries for electronic structure programs. *Comput. Phys. Commun.* **182**, 1183–1186 (2011).
44. Dal Corso, A. Pseudopotentials periodic table: from H to Pu. *Comput. Mater. Sci.* **95**, 337–350 (2014).
45. Mostofi, A. A. et al. An updated version of wannier90: a tool for obtaining maximally localised Wannier functions. *Comput. Phys. Commun.* **185**, 2309–2310 (2014).
46. Ozaki, T. et al. OpenMX: open source package for Material eXplorer (2019); http://www.openmx-square.org/
47. Morrison, I., Bylander, D. M. & Kleinman, L. Nonlocal Hermitian norm-conserving Vanderbilt pseudopotential. *Phys. Rev. B* **47**, 6728–6731 (1993).
48. Theurich, G. & Hill, N. A. Self-consistent treatment of spin-orbit coupling in solids using relativistic fully separable ab initio pseudopotentials. *Phys. Rev. B* **64**, 073106 (2001).
49. Ozaki, T. Variationally optimized atomic orbitals for large-scale electronic structures. *Phys. Rev. B* **67**, 155108 (2003).
50. Nishino, Y. et al. Semiconductor like behavior of electrical resistivity in Heusler-type Fe_2VAl compound. *Phys. Rev. Lett.* **79**, 1909–1912 (1997).
51. Matyunina, M., Zagrebin, M., Sokolovskiy, V. & Buchelnikov, V. Ab initio study of magnetic and structural properties of Fe-Ga alloys. *EPJ Web Conf.* **185**, 04013 (2018).
52. Lechermann, F. et al. Density-functional study of Fe_3Al: LSDA versus GGA. *Phys. Rev. B* **65**, 132104 (2002).
53. Paduani, C. & Bormio-Nunes, C. Density functional theory study of Fe_3Ga. *J. Appl. Phys.* **109**, 033705 (2011).

Acknowledgements We thank T. Tsujikawa for assistance with thin-film fabrication. This work is partially supported by CREST (JPMJCR18T3), New Energy and Industrial Technology Development Organization (NEDO), PRESTO (JPMJPR15N5), Japan Science and Technology Agency, by Grants-in-Aids for Scientific Research on Innovative Areas (JP15H05882 and JP15H05883) from the Ministry of Education, Culture, Sports, Science, and Technology of Japan, and by Grants-in-Aid for Scientific Research (JP16H02209, JP16H06345, JP19H00650) from the Japanese Society for the Promotion of Science (JSPS). The work at IQM was supported by the US Department of Energy, Office of Basic Energy Sciences, Division of Materials Sciences and Engineering under grant DE-FG02-08ER46544. The work for first-principles calculations was supported in part by JSPS Grant-in-Aid for Scientific Research on Innovative Areas (JP18H04481 and JP19H05825) and by MEXT as a social and scientific priority issue (Creation of new functional devices and high-performance materials to support next-generation industries) to be tackled by using post-K computer (hp180206 and hp190169). The use of the facilities of the Materials Design and Characterization Laboratory at the Institute for Solid State Physics, The University of Tokyo, is acknowledged.

Author contributions A.S., S. Minami, T.K., T.C. and T.H. contributed equally to this work. S.N. and R.A. conceived the project. S.N. planned the experiments. T.K. performed the high-throughput computational search. T.C. and Y.W. worked on the single-crystal growth and the preparation of samples. A.S., T.C. and Y.W. carried out the transport and magnetization measurements and analysed the data. T.H. and S. Miwa fabricated the thin film and performed its structural and chemical analyses and transport measurement. S. Minami, T.K., F.I., T.N., M.H. and R.A. performed the first-principles calculations. D.S.-H. performed chemical analyses and took the electron diffraction image. S.N., R.A., A.S., S. Minami, T.K., T.H. and F.I wrote the paper. All authors discussed the results and commented on the manuscript.

Competing interests The authors declare no competing interests.

Additional information
Supplementary information is available for this paper at https://doi.org/10.1038/s41586-020-2230-z.
Correspondence and requests for materials should be addressed to S.N.
Peer review information *Nature* thanks Ernst Bauer and the other, anonymous, reviewer(s) for their contribution to the peer review of this work.
Reprints and permissions information is available at http://www.nature.com/reprints.

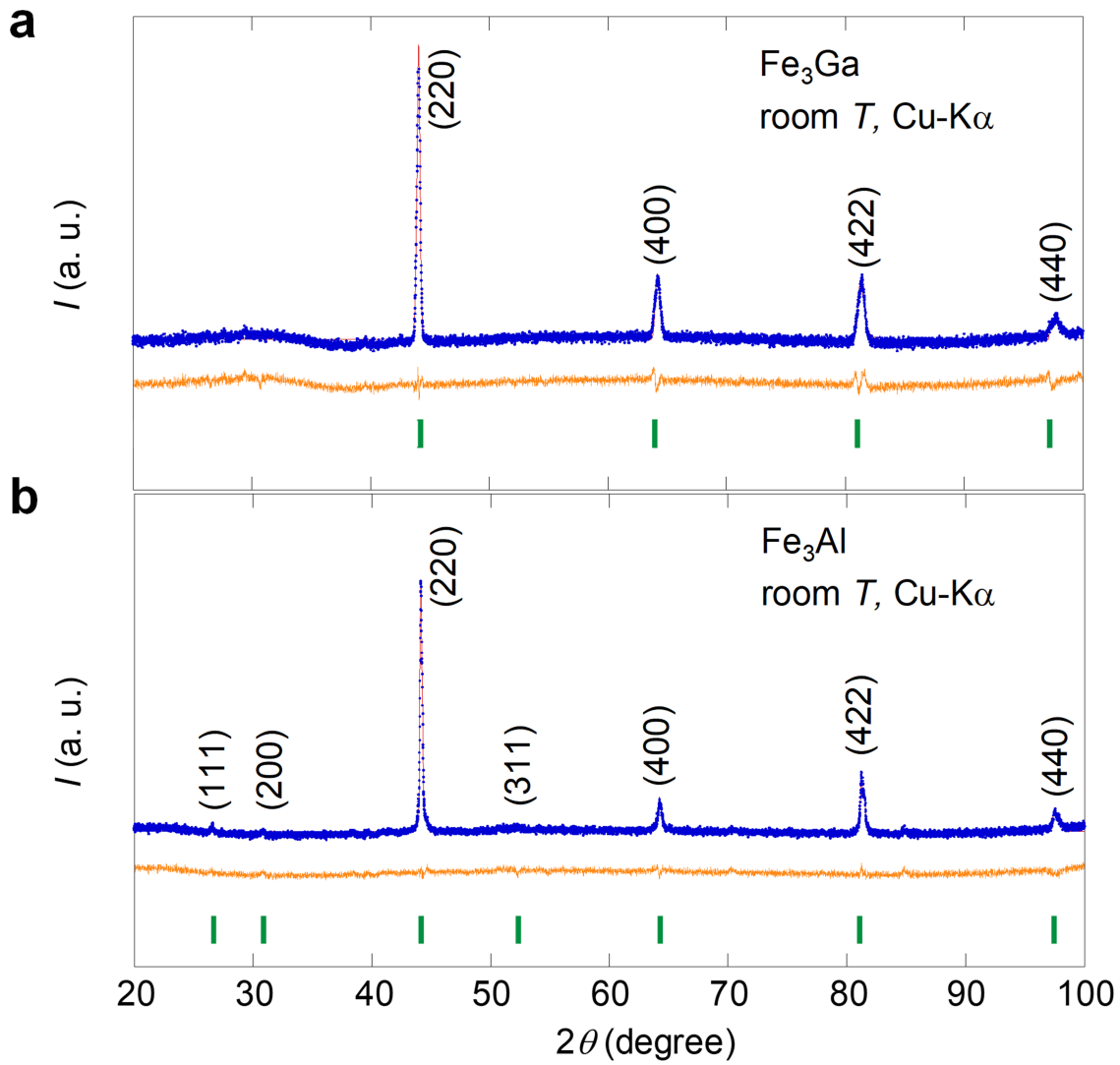

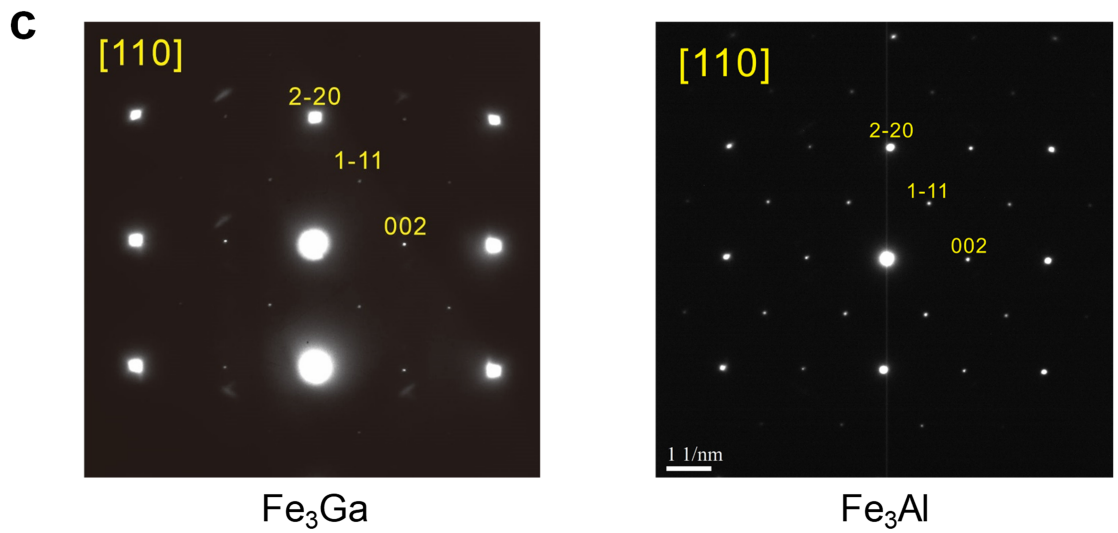

Extended Data Fig. 1 | Evidence for the DO_3 structure of Fe_3X. a, **b**, XRD pattern for Fe_3Ga (**a**) and Fe_3Al (**b**) obtained by Cu-Kα radiation ($\lambda = 1.5401$ Å) at room temperature. The solid circles and the solid line (red) represent the experimental results and the Rietveld refinement fit, respectively. The final weighted and expected R indicators and goodness-of-fit indicator S are $R_{WP} = 2.34\%$, $R_e = 1.49\%$ and $S = 1.55$ for Fe_3Ga and $R_{WP} = 1.91\%$, $R_e = 1.27\%$ and $S = 1.48$ for Fe_3Al, respectively. Vertical bars (green) below the curves indicate the major peak positions calculated for DO_3 Fe_3Ga and Fe_3Al, which are more than 1% of the main peak. The lower curve (orange) represents the difference between the experimental result and the Rietveld refinement. I, intensity. **c**, Selected area electron diffraction pattern for our single crystals of Fe_3Ga (left) and Fe_3Al (right) taken from the [110] plane.

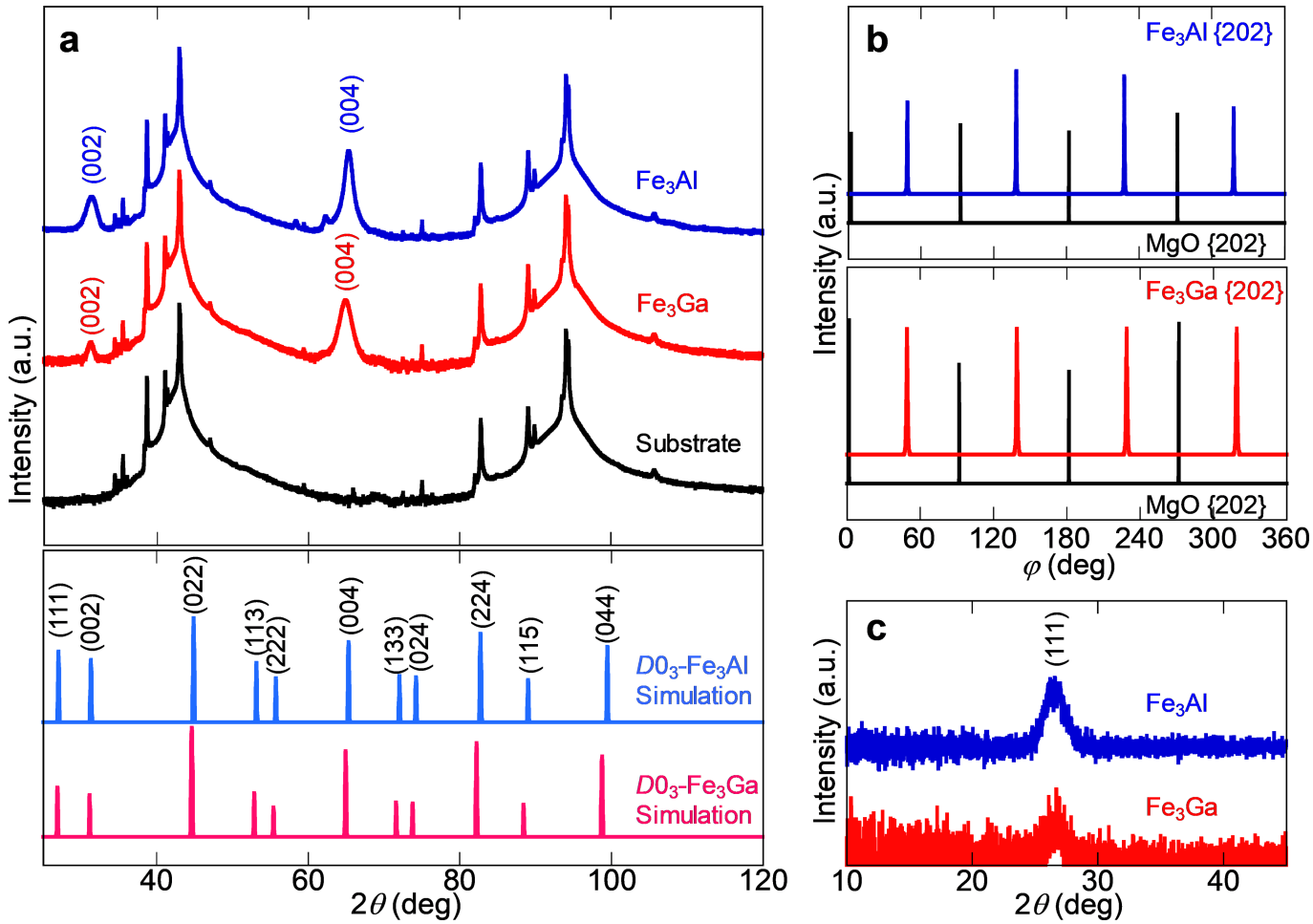

Extended Data Fig. 2 | Evidence for $D0_3$ structure of Fe3Ga and Fe_3Al thin films. a, Room temperature spectra obtained by XRD $2\theta/\omega$-scans for the Fe_3X thin films on an MgO substrate and the MgO substrate itself. The theoretical simulation patterns for the $D0_3$ Fe_3Ga and Fe_3Al structures are presented at the bottom. **b**, φ-scan patterns of the {202} planes of the Fe_3Ga and Fe_3Al layers, and the MgO substrate. **c**, $2\theta/\omega$-scan patterns for the (111) plane of the Fe_3Ga and Fe_3Al thin-film layers.

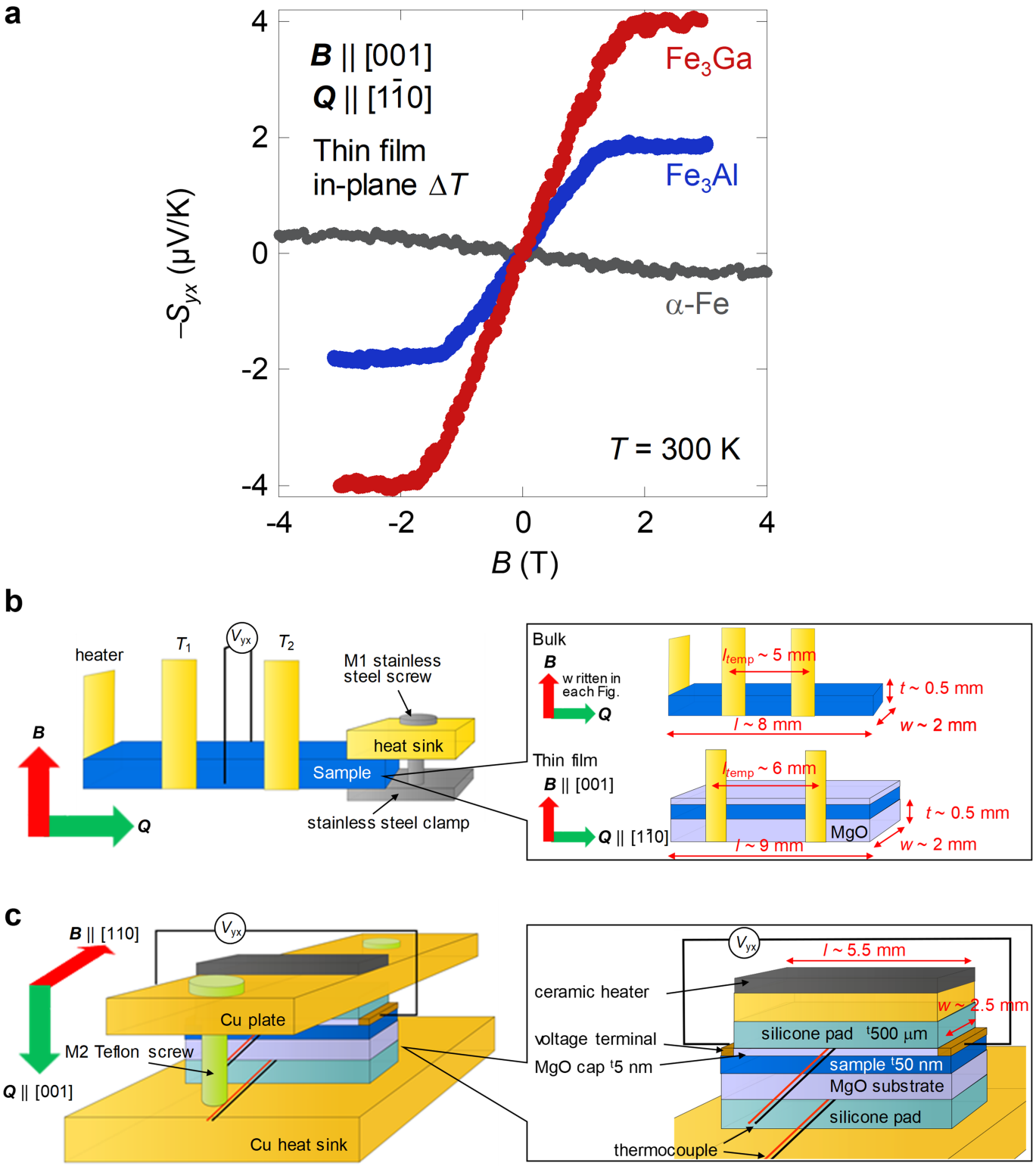

Extended Data Fig. 3 | ANE of Fe_3X and experimental setup for both bulk and thin films. a, Magnetic field dependence of the ANE obtained for the Fe_3X thin films (50 nm) and the α-Fe thin film (50 nm) using the in-plane temperature gradient. **b**, Schematic of the experimental setup for the ANE measurement using the in-plane temperature gradient. **c**, Schematic of the experimental setup for the ANE measurement using the out-of-plane temperature gradient.

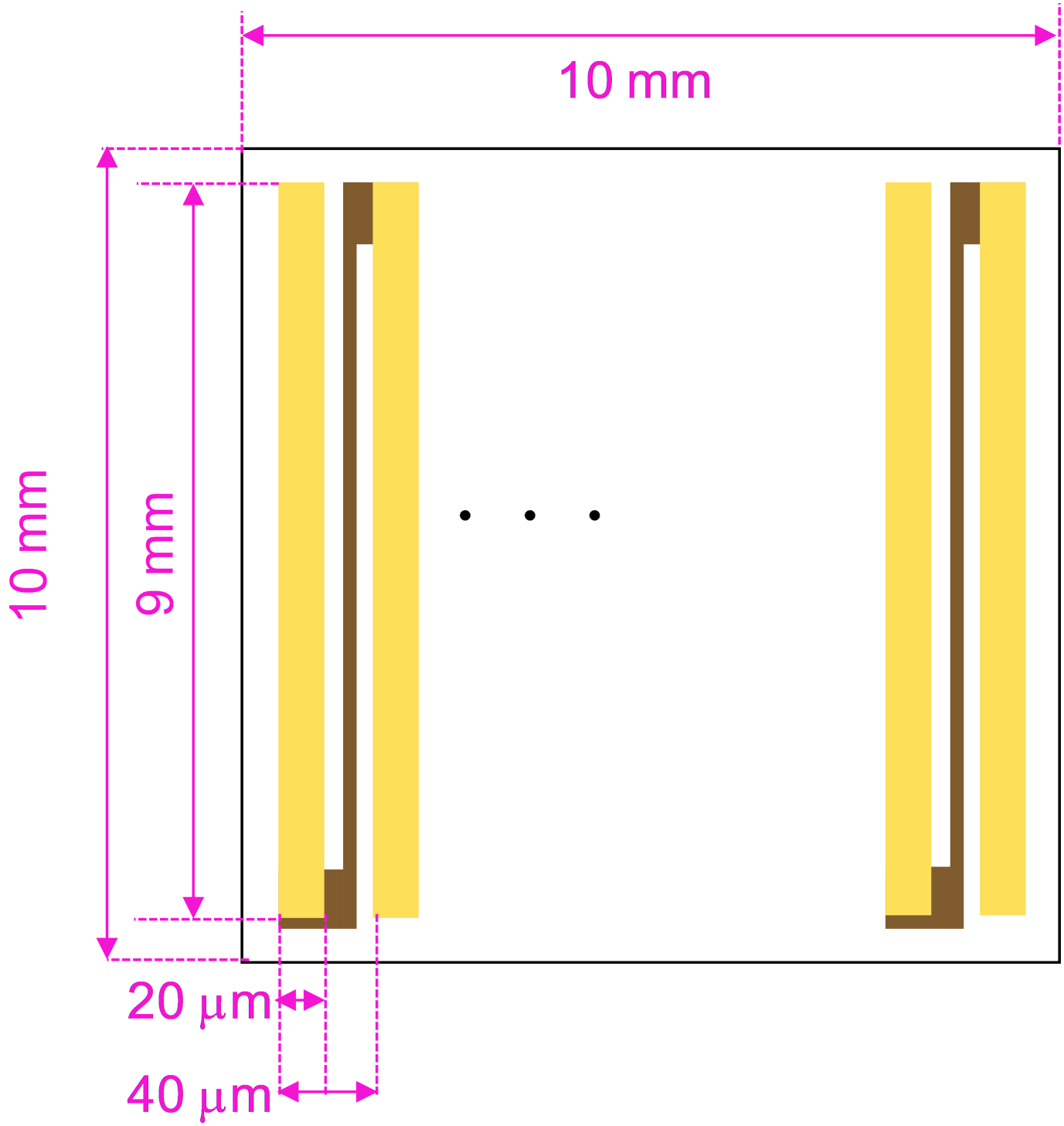

Extended Data Fig. 4 | Schematic of the μ-TEG based on the ANE. The thermopile consists of a square-shaped substrate (black frame) and an alternating array of Fe_3X (yellow) and gold wires (brown) placed on the substrate and these two wires are connected in a zigzag configuration. A temperature gradient is applied perpendicular to the plane. The thickness of the wire is designed to be 1 μm.

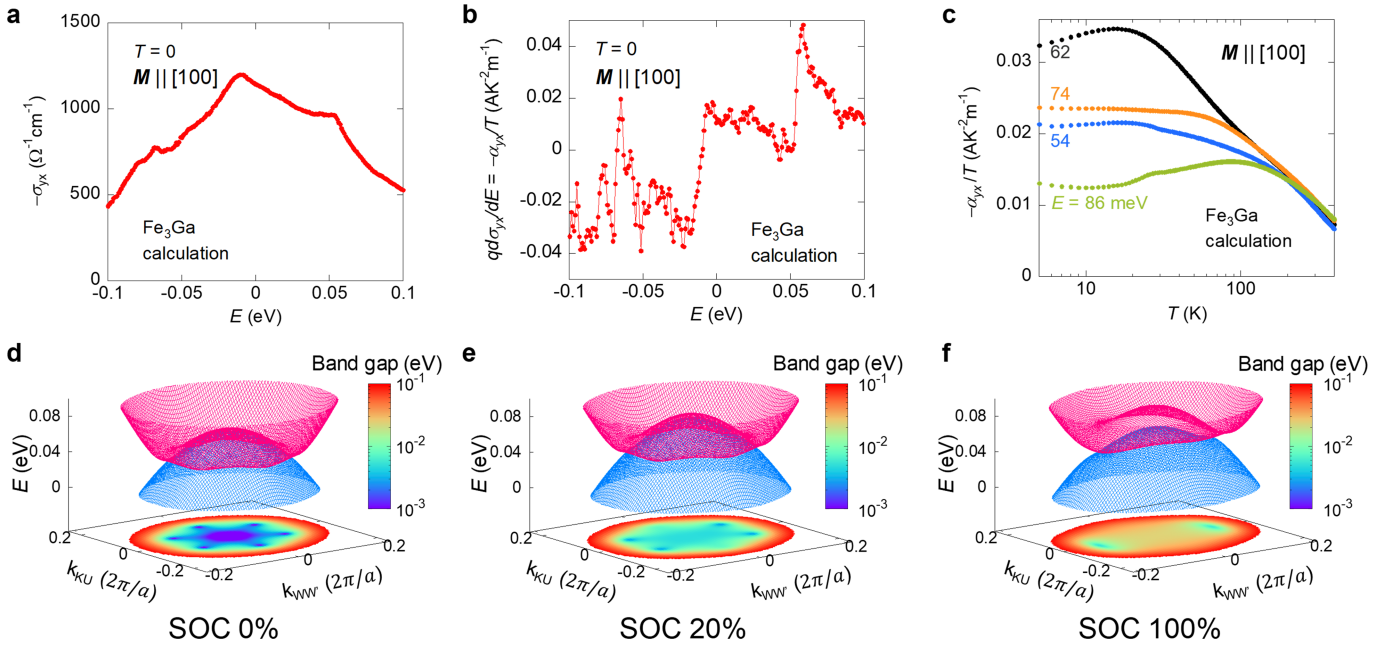

Extended Data Fig. 5 | Energy dependence of the Hall conductivity and transverse thermoelectric conductivity, and the effect of the SOC on the nodal web structure. a, Energy dependence of $-\sigma_{yx}$ obtained from the first-principles calculations at $T = 0$. **b**, Energy dependence of $-\alpha_{yx}/T$ calculated based on the Mott relation (Methods). **c**, Temperature dependence of $-\alpha_{yx}/T$ at various energies. **d**–**f**, Band structure of the nodal web around the L point for different strengths of the SOC: 0% (**d**), 20% (**e**) and 100% (**f**). We also show the contour plot of the bandgap in the k_{KU}–$k_{WW'}$ plane.

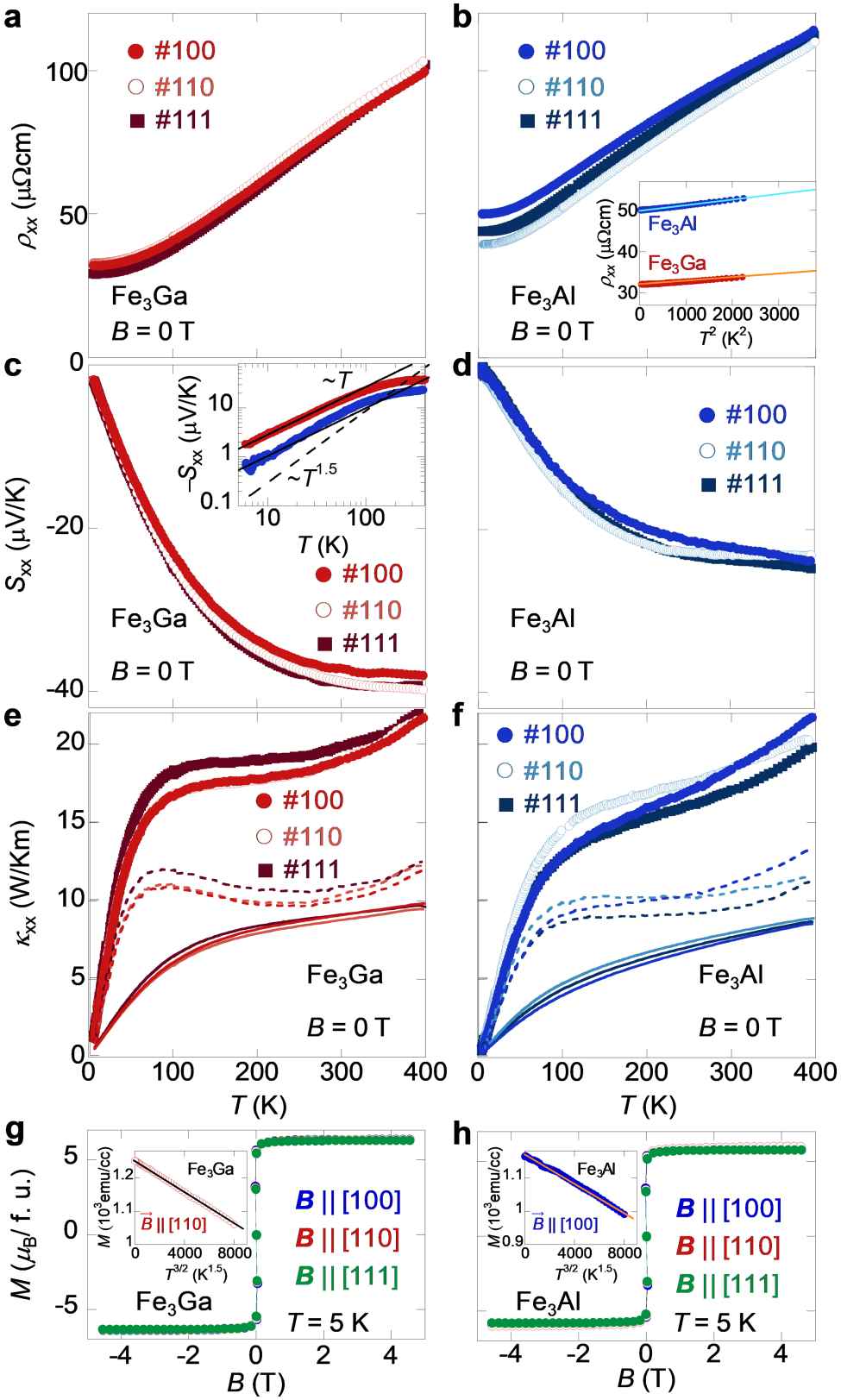

Extended Data Fig. 6 | Longitudinal electric and thermal transport properties and magnetization for Fe_3X. a, **b**, Temperature dependence of the longitudinal resistivity ρ_{xx} for Fe_3Ga (**a**) and Fe_3Al (**b**). **c**, **d**, Temperature dependence of the Seebeck coefficient S_{xx} for Fe_3Ga (**c**) and Fe_3Al (**d**). **e**, **f**, Temperature dependence of the thermal conductivity κ_{xx} for Fe_3Ga (**e**) and Fe_3Al (**f**). #100, #110 and #111 represent the samples used for the transport measurements in **B** || [100], [110] and [111], respectively. The inset in **b** shows the T^2 dependence of ρ_{xx} for Fe_3Ga #100 (red) and Fe_3Al #100 (blue). The inset in **c** shows the log–log plot of $-S_{xx}$ versus T for Fe_3Ga #100 (red) and Fe_3Al #100 (blue). The solid and broken lines represent the T and $T^{1.5}$ dependence, respectively. The solid and broken lines in **e** and **f** show the estimated electric and lattice contributions to the thermal conductivity (Supplementary Information). **g**, **h**, Magnetization curve for Fe_3Ga (**g**) and Fe_3Al (**h**) at $T = 5$ K under **B** || [100], [110] and [111]. The insets in **g** and **h** are the $T^{3/2}$ dependence of $M(T)$.

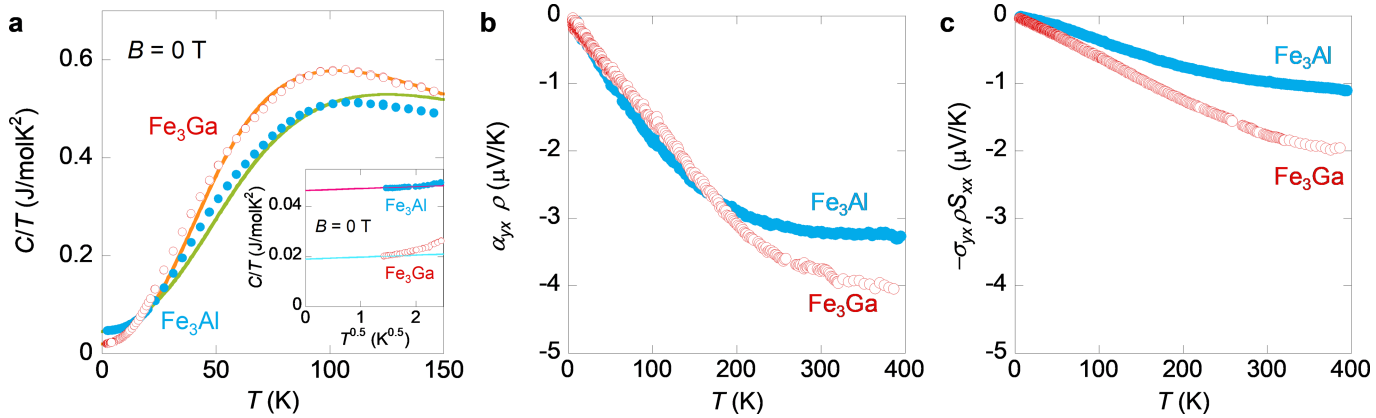

Extended Data Fig. 7 | Specific heat and two contributions to the anomalous Nernst effect. a, Temperature dependence of the specific heat divided by temperature C/T for Fe_3X. The solid lines represent the fit by the combination of the electronic and Debye-type phonon specific heat and ferromagnetic magnon contribution (Supplementary Information). The inset shows the $T^{1/2}$ dependence of C/T at low temperatures. **b**, **c**, $\alpha_{yx}\rho$ (**b**) and $-\sigma_{yx}\rho S_{xx}$ (**c**). The ANE is the sum of the two terms, that is, $S_{yx} = \alpha_{yx}\rho - \sigma_{yx}\rho S_{xx}$ (Supplementary Information).

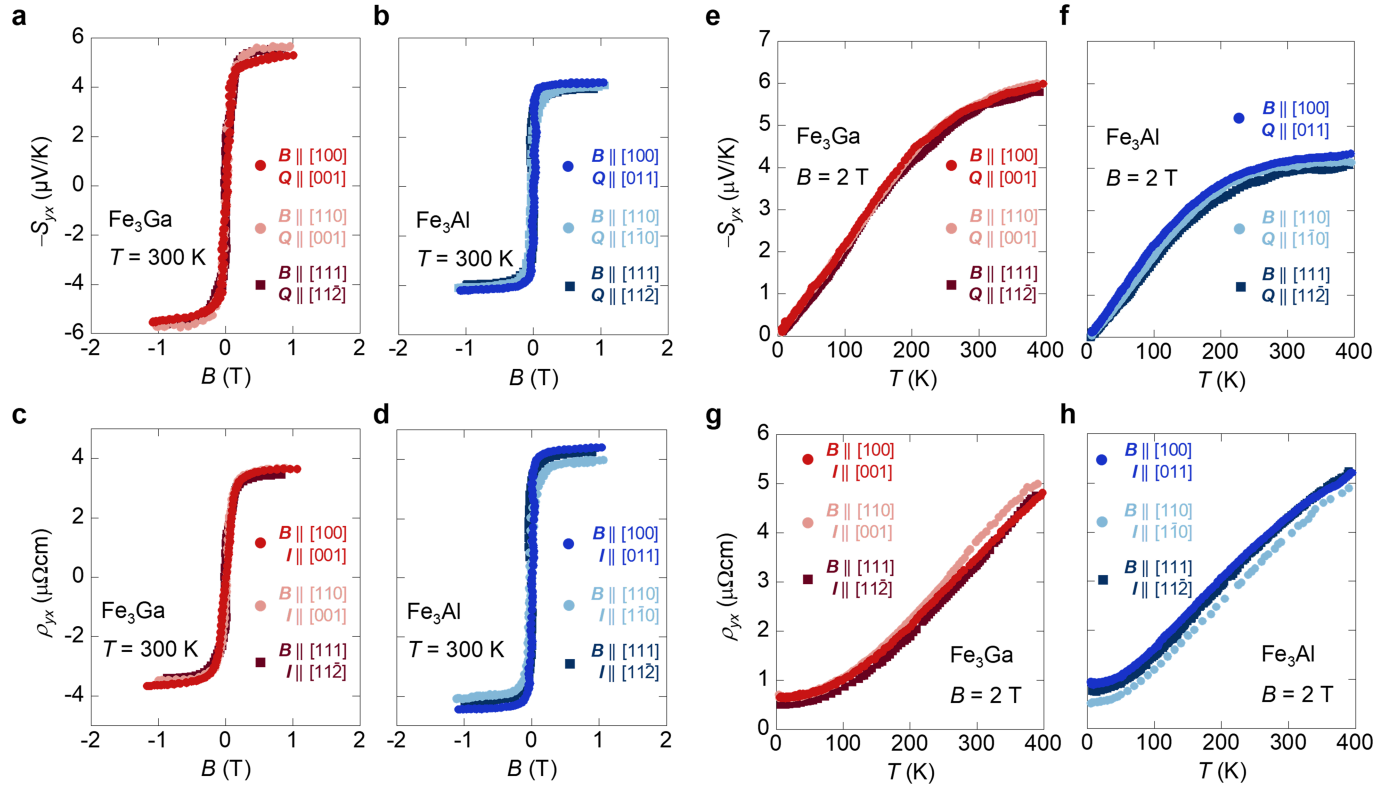

Extended Data Fig. 8 | Anisotropy in the Nernst coefficient and Hall resistivity. a–**d**, Magnetic field dependence of the Nernst coefficient $-S_{yx}$ for Fe_3Ga (**a**) and Fe_3Al (**b**), and the Hall resistivity ρ_{yx} for Fe_3Ga (**c**) and Fe_3Al (**d**) in **B** || [100], [110] and [111]. **e**–**h** Temperature dependence of $-S_{yx}$ for Fe_3Ga (**e**) and Fe_3Al (**f**), and ρ_{yx} for Fe_3Ga (**g**) and Fe_3Al (**h**) in **B** || [100], [110] and [111].

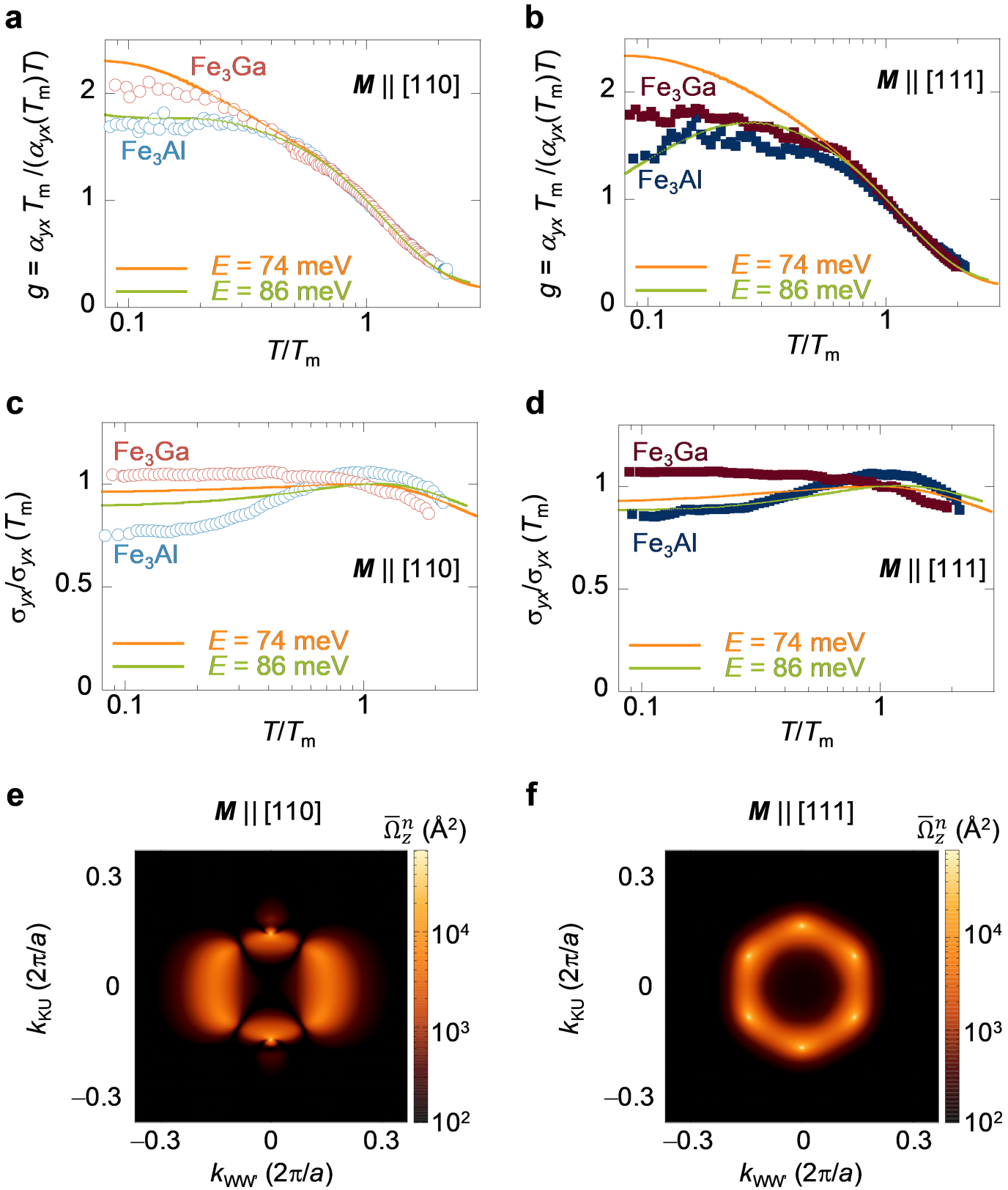

Extended Data Fig. 9 | Anisotropy in the transverse thermoelectric conductivity $-\alpha_{yx}$, Hall conductivity $-\sigma_{yx}$ and Berry curvature. a, **b**, Scaling relation of $-\alpha_{yx}$ for **M** || [110] (**a**) and **M** || [111] (**b**) versus T/T_m. **c**, **d**, Scaling relation of $-\sigma_{yx}$ for **M** || [110] (**c**) and **M** || [111] (**d**) versus T/T_m. The solid lines in **a**–**d** are obtained by the first-principles calculations. The scaling parameters used here are summarized in Extended Data Table 1. Details are the same as Fig. 3c, d for **M** || [100] in the main text. **e**, **f**, Contour plot of the Berry curvature $\Omega_{n,z}$ of the lower-energy band n in the vicinity of the nodal web structure around the L point for **M** || [110] (**e**) and **M** || [111] (**f**). Details are the same as Fig. 4e for **M** || [100] in the main text.

Extended Data Table 1 | List of the scaling parameters and magnitude of σ_{yx} and σ_{xx} at $T \approx 0$

	M	T_m	$-\alpha_{yx}(T_m)$	$-\sigma_{yx}(T_m)$	$\lvert\sigma_{yx}(T \sim 0)\rvert$		$\lvert\sigma_{xx}(T \sim 0)\rvert$	
unit	-	K	$AK^{-1}m^{-1}$	$\Omega^{-1}cm^{-1}$	$\Omega^{-1}cm^{-1}$	$e^2/(2ha)$	$\Omega^{-1}cm^{-1}$	$e^2/(2ha)$
Fe_3Ga	[100]	200	5.2	610	~600	~0.9	~31000	~47
	[110]	210	5	570				
	[111]	200	5.1	550				
Fe_3Al	[100]	180	3.6	460	~370	~0.55	~20000	~30
	[110]	180	3.8	460				
	[111]	180	3.3	460				
74 meV	[100]	320	3.3	730				
	[110]	340	2.8	610				
	[111]	340	2.7	590				
86 meV	[100]	370	3.3	670				
	[110]	370	2.8	560				
	[111]	380	2.7	540				

The first two rows indicate the experimental values obtained for Fe_3Ga and Fe_3Al and the last three rows the theoretical values obtained for $E = +74$ and $E = +86$ meV. Each has three consecutive rows corresponding to the orientation of the magnetization. Here, T_m is the temperature where the transverse thermoelectric conductivity $|\alpha_{yx}|$ attains its maximum $|\alpha_{yx}(T_m)|$.